Received: 8 December 2022 | Revised: 27 February 2023 | Accepted: 19 March 2023

High Voltage

DOI: 10.1049/hve2.12335

国家电网 STATE GRID 中国电力科学研究院有限公司 CHINA ELECTRIC POWER RESEARCH INSTITUTE | IET The Institution of Engineering and Technology | WILEY

REVIEW

Recent advances in multipactor physics and mitigation

Asif Iqbal[1] | De-Qi Wen[1,2] | John Verboncoeur[1,2] | Peng Zhang[1]

[1]Department of Electrical and Computer Engineering, Michigan State University, East Lansing, Michigan, USA

[2]Department of Computational Mathematics, Science, and Engineering, Michigan State University, East Lansing, Michigan, USA

Correspondence
Peng Zhang.
Email: pz@egr.msu.edu

Associate Editor: Cheng Zhang

Funding information
Air Force Office of Scientific Research, Grant/Award Numbers: FA9550-18-1-0062, FA9550-21-1-0367; Multidisciplinary University Research Initiative

Abstract

Recent progress made in the prediction, characterisation, and mitigation of multipactor discharge is reviewed for single- and two-surface geometries. First, an overview of basic concepts including secondary electron emission, electron kinetics under the force law, multipactor susceptibility, and saturation mechanisms is provided, followed by a discussion on multipactor mitigation strategies. These strategies are categorised into two broad areas – mitigation by engineered devices and engineered radio frequency (rf) fields. Each approach is useful in different applications. Recent advances in multipactor physics and engineering during the past decade, such as novel multipactor prediction methods, understanding space charge effects, schemes for controlling multipacting particle trajectories, frequency domain analysis, high frequency effects, and impact on rf signal quality are presented. In addition to vacuum electron multipaction, multipactor-induced ionization breakdown is also reviewed, and the recent advances are summarised.

1 | INTRODUCTION

Multipactor [1–5] is a nonlinear phenomenon that occurs when electrons driven by a high frequency electric field in a high vacuum environment create an avalanche by impacting one or more metallic [2] or dielectric [3, 6, 7] surfaces. The electron avalanche sustains itself by a rapid charge growth through secondary electron emission [8–11] from the surfaces and can cause a multitude of problems in radio frequency (rf) and microwave systems, such as satellite communication payloads and spacecraft components [12–14], travelling wave tubes (TWTs) [15], high power microwave sources [16], and particle accelerators [17–19]. These problems include the breakdown of dielectric windows [20–23], erosion of metallic structures, melting of internal components, and perforation of vacuum walls [2]. In addition, multipactor can often detune rf systems, cause multitone coupling and signal distortion [24], limit the transmission or delivery of rf power, and cause a local pressure rise due to the desorption of surface gases [25]. In particle accelerators such as the Large Hadron Collider (LHC) multipactor has been found to be responsible for problems including the rise of pressure inside the beam pipes, heat loads, and beam instabilities [18, 19, 26]. Although there are some beneficial applications of multipactor discharge [3], its various undesirable effects often far outweigh the useful aspects. Mitigation of multipactor has been one of the major challenges for the rf community over the past few decades. Besides multipactor in rf environments (as we will focus in this paper), dc multipactor [27] also exists and is an important problem in the power and energy community in high voltage dc, which is also of importance in solar and wind sources, high voltage inverters, including in space systems.

The earliest studies on multipactor discharge can be traced back to 1920s when French physicists C. Gutton and H. Gutton reported the phenomenon in a series of publications [28]. In 1934, Philo T. Farnsworth first referred to this phenomenon as "multipactor" [1] and designed an electron multiplier tube capable of employing multipactor to produce a television image. He received several patents on technologies which highlighted multipactor discharges [29–32]. Gill and von Engel of Oxford University conducted theoretical and experimental studies providing a theoretical relation between the amplitude, phase, and frequency of the driving field, and the multipactor trajectory

Asif Iqbal and De-Qi Wen contributed equally to this study.

length [33]. In 1950's, Hatch and Williams reformulated [34, 35] the theory within a more concise mathematical framework with the help of a number of multipactor breakdown experiments. In later decades, multipactor research proliferated in all types of rf devices. Notably, in 1961, independent experiments conducted by Vaughan [20, 21], and Priest and Talcott [20] led to the discovery of the single surface multipactor which is responsible for dielectric window failure in magnetrons and klystrons. In these experiments, multipactor was manifested in the form of excessive heating as well as cracking and puncturing of the dielectric window due to the electrostatic charging of an evaporated metallic deposit on the surface. Multipactor therefore grew as a major concern in diverse rf applications rendering a comprehensive understanding of the phenomenon essential.

Early theoretical treatments of multipactor [33–36] were based on simple assumptions such as negligible space charge effects, monoenergetic secondary electrons, emission normal to surfaces, etc. In a widely employed early theory [33], Gill and von Engel introduced the ad hoc assumption that the ratio of the impact velocity of the primary electrons to the emission velocity of secondaries is a constant parameter denoted by k. However, in the 1980's, Vaughan [2] promoted an alternative theory from first principles and employed it to accurately predict multipactor breakdown conditions in a parallel plate geometry. The theory was adopted by many researchers in the 1990's and 2000's such as Riyopoulos *et al.* [37–39], Kishek *et al.* [4, 40–42], Ang. *et al.* [43], and Valfells *et al.* [44, 45] etc. More recently, N. K. Vdovicheva *et al.* and S. Anza *et al.* have developed alternatives to the classical theory of electron dynamics called nonstationary and quasi-stationary statistical theories [46–54] for both two surface and single surface multipactor with experimental validation. Siddiqi and Kishek proposed a map based theory [55, 56] based on principles from nonlinear dynamics and chaos theory to study multipactor discharge. Semi-empirical multicarrier multipaction threshold prediction methods, such as the widely employed "20 gap crossing rule", have been adopted in the industry [57].

In addition to these analytical theories, advanced computational capabilities in recent decades have enabled researchers to improve on the modelling assumptions and tackle more realistic physical conditions in diverse device geometries by employing Monte Carlo (MC) [6, 43, 58–60] and particle-in-cell (PIC) simulations [61]. Computational studies of multipactor are summarised in the review articles of Kishek [3] and Iqbal [62]. Also noteworthy is that in recent years, along with numerical and analytical studies, much emphasis has been put on computer aided simulations of multipactor discharge using software such as MSAT (Multipactor Simulation and Analysis Tool) [63, 64], MEST (Multipactor Electron Simulation Tool) [65, 66], FEST-3D (Finite-volume Explicit STructured 3-Dimensional) [67, 68], Spark3D [69], and CST (Computer Simulation Technology) [70–73].

Besides the electron avalanche induced under high vacuum conditions, multipactor discharges can also lead to a volume breakdown and the formation of an rf plasma. Initially, most studies were conducted via experimental measurements, focussing on the current, luminosity, soft X-ray emission, transmission and reflected microwave power, as well as spectroscopy of excited atoms that confirms the presence of desorbed gas from the surface [74, 75]. Computational models, especially kinetic PIC simulations that can reveal the nonlinear multiphysics discharge dynamics, provided better understanding of the complicated plasma breakdown process in recent years [76–79].

In this paper, fundamental theories of multipactor discharge are revisited with brief explanations. In Section 2, the fundamental concepts, including secondary electron emission, electron kinetics under the force law, multipactor susceptibility and saturation, are introduced for single- and two-surface geometries. Recent advances in mitigation including engineering the devices as well as the driving rf fields are surveyed in Section 3 with the consideration of their specific scopes of applicability. In Section 4, recent advances in multipactor physics and engineering, such as controlling secondary electron emission through electrode surface morphology, breakdown characteristics, novel multipactor prediction methods, space charge effects, schemes of controlling multipacting particle trajectories, frequency domain analysis, multipactor at high frequency, and its impact on signal quality are discussed. The findings from experiments, theoretical models, as well as fully kinetic PIC simulations to study multipactor and its transition to volume plasma breakdown are reviewed in Section 5. Conclusion and outlook are given in Section 6.

2 | MULTIPACTOR BASICS

In this section, firstly, we briefly describe the electron-induced secondary electron emission process for electron bombardment on a solid surface made of metal or dielectric that elucidates the origin of the shape of secondary electron yield (SEY) curve. Then, we introduce the principle of two-surface and single-surface multipactor discharge, in the chronological order in which they were first discovered and investigated. We also discuss multipactor in coaxial lines and complex geometries.

2.1 | Secondary electron yield

Electron-induced secondary electron emission enables multipactor discharges as the maximum secondary electron yield (SEY) due to impact of primary energetic electrons can be above unity, leading to an exponential growth process. The well-known empirical Vaughan's formula [10, 80] that describes SEY as a function of the primary electron energy and impact angle is commonly adapted in the microwave community. The physics behind the SEY is usually neglected in multipactor studies. Here, before discussing the multipactor discharges and breakdown, we first briefly introduce the physical process of secondary electron emission.

The secondary electron emission process can be described by a three-step process (for a more detailed discussion see [81]), that is, penetration of the primary electrons into the solid surface and transfer energy to excite free secondary electrons, internal

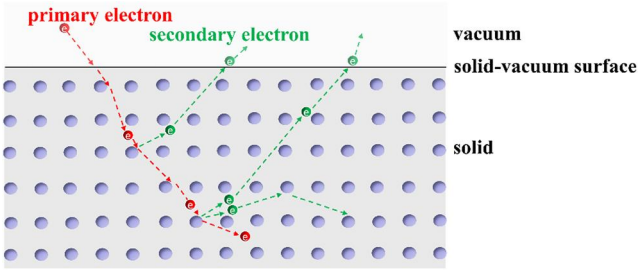

FIGURE 1 A schematic for primary electron-induced secondary electron emission process.

secondary electron scattering through the material, and secondary electron escape through the solid-vacuum interface. A schematic describing this process is shown in Figure 1. The higher energy the primary electrons have, the longer trajectory they can travel after plunging into the solid material (metal or dielectric). The primary electrons slow down through collisions with free electrons and the lattice in the solid and transfer kinetic energy to internally generated secondary electrons. If the primary electrons have a higher velocity, then they have a shorter time to interact with the lattice electrons, thus, the internal yield per unit length is low. As the primary electrons slow down, the interaction time increases, and the yield per unit length increases. The internal secondary electrons transport inside the solid, and the probability of ejection from the solid exponentially decreases as a function of the distance away from the surface. As a combined effect, at low primary electron energy, the internal secondary electrons can escape from the solid very efficiently. With increasing primary electron energy, the number of internal secondary electrons increases, because the interaction length of the primary electron with the solid is longer, resulting in a higher SEY at higher primary electron energy. However, when the primary electron energy is very high, the exponential reduction nature of escape probability of internal secondary electrons results in a more rapid decrease of secondary electron emission than the increase in generation of internal secondary electrons. Consequently, SEY increases with the primary electron energy first and then decrease after a maximum SEY at a certain primary electron energy around a few hundred eV for many known materials. It can be inferred that the primary electron-solid interaction processes are different for different materials, and consequently the secondary yield curves vary by material.

In the microwave community, workers extensively use Vaughan's empirical formula fitting experimental measurements rather than considering the complicated processes above. Vaughan's formula for SEY (δ) for an incident primary electron with an energy of E_i is as follows [10, 80]:

$$\delta(E_i) = \begin{cases} \delta_{max}\left(we^{1-w}\right)^k; & \text{for } w \le 3.6 \\ \delta_{max}\left(1.125/w^{0.35}\right); & \text{for } w > 3.6 \end{cases} \quad (1)$$

where $k = 0.56$ for $w < 1$ and $k = 0.25$ for $1 \le w \le 3.6$, $w = (E_i - E_0)/(E_{max} - E_0)$, and E_0 is the threshold impact energy below which the SEY is zero. For an impact angle θ with respect to the normal vector of the surface, E_{max} and δ_{max} are:

$$E_{max} = E_{max0}\left(1 + \frac{k_s\theta^2}{2\pi}\right) \quad (2)$$

$$\delta_{max} = \delta_{max0}\left(1 + \frac{k_s\theta^2}{2\pi}\right) \quad (3)$$

As a result, the overall SEY curve can be determined by the maximum SEY for normal incidence of primary electrons, δ_{max0}, and the corresponding primary electron impact energy for normal incidence, E_{max0}. The two crossover energies, E_1 and E_2, are defined as energies at which the SEY is unity (Figure 2). For oblique incidence, the penetration depth of a primary electron in the normal direction of a surface is smaller, thus the generated internal secondary electrons are more likely to escape, and the SEY is higher. Figure 2 is a typical SEY curve [6] showing the dependence of SEY on primary impact energy.

In addition to Vaughan's formula, there are other models for SEY calculation in the literature. For example, the more sophisticated Furman's SEY model is widely used in the particle accelerator community. Furman's model requires 47 parameters to characterise the SEY properties, which is much more complicated than Vaughan's model. A comparison of these two models can be seen in [82]. The SEY can also be calculated by density functional theory coupled with Monte Carlo simulations, and such methods are more complicated and also time-consuming in calculation compared to Vaughan's model. More details can be found in [83].

2.2 | Two-surface multipactor

The first major breakthrough in understanding the physics of the multipactor phenomenon came in 1936 when Henneburg *et al.* [36] described the electron dynamics of two surface multipactor and derived the resonance condition on the transit time for electrons emitted with zero initial velocity. In the following decades, two surface multipactor has been extensively studied and the field has been developing continuously. In what follows we present the basic concepts of two surface multipactor, that is, the electron dynamics, resonance condition, multipactor modes, and saturation.

Figure 3 depicts the schematic of two surface multipactor discharge in the presence of an electric field consisting of a single frequency component. An rf electric field $E_y = E_{rf}\sin(\omega t + \theta)$ is acting normal to the parallel plates A and B along the y-direction. Here E_{rf} is the peak electric field strength, ω is the angular frequency, and θ is the initial phase of the electric field. In Figure 3a, an electron is emitted from plate A and then accelerated by the RF electric field. Assuming one-dimensional (1D) motion in the y-direction, the flight trajectory of a multipactor electron is governed by the force law [2, 25, 84],

$$a(t) = -\frac{eE_{rf}}{m}\sin(\omega t + \theta) = -\frac{eV_{rf}}{md}\sin(\omega t + \theta), \quad (4)$$

where $a(t)$ is the acceleration, V_{rf} is the peak voltage, and d is the gap distance between plates A and B. The instantaneous position of a multipactor electron is obtained as,

$$y = -\frac{eV_{rf}}{m\omega^2 d}(\omega t \cos\theta - \sin(\omega t + \theta) + \sin\theta) + v_0 t + y_0 \quad (5)$$

Here v_0 and y_0 account for initial velocity and position of the particles at $t = 0$, respectively. The transit time τ_{AB} of an electron in flight from plate A to plate B, is calculated by solving Equation (5) for $y = d$.

The multipactor resonance condition [2, 84] specifies that the electron must traverse the electrode spacing, d, and impact the opposing surface near the time the electric field changes direction. The electric field changes direction at $\omega t = N\pi + \theta$, where N is a positive odd integer, that is, $y = d$ at $\omega t = N\pi + \theta$. Invoking this condition in Equation (5), the multipactor condition for the voltage in a parallel plate geometry is given by,

$$V_{rf} = -\frac{m}{e}\frac{\omega d(\omega d - v_0 N\pi)}{N\pi\cos\theta + 2\sin\theta}. \quad (6)$$

The positive odd integer, N, is called the multipactor mode or multipactor order. The minimum voltage necessary to sustain a multipactor will occur at the phase, $\theta = \arctan\left(\frac{2}{N\pi}\right)$, that maximises the denominator in Equation (6) regardless of the value of v_0 [2, 84]. The maximum voltage allowed to sustain a multipactor will occur with the maximum negative value of the angle θ, determined by the condition that the initial emission velocity v_0 just allows the electron to escape from its birth electrode against the initially retarding field [2, 84]. The impact velocities corresponding to the first and second crossover incident energies in the SEY curve (discussed in Section 2.1) lead to two more constraints [85] on the values of the rf voltage that can lead to multipactor.

Multipactor susceptibility in a two-surface geometry is usually represented in a contour plot in the (V_{rf}, fd) parameter space called the multipactor susceptibility diagram (Figure 4). The boundaries in the susceptibility diagram correspond to the extremum rf voltage values that can lead to multipactor discharge, as discussed above.

In 1995, Kishek and Lau showed [40] that the rapid initial growth of multipactor current is followed by a saturation state resulting from the loading of the rf cavity. In the saturation state, the ensemble averaged (effective) SEY over an rf period tends to unity. Later, through detailed particle simulations, Spilios Riyopoulos found [37] that two synergistic effects lead to multipactor saturation. First, the mutual repulsion disperses the electron bunch causing a significant fraction of the impact phases to spill over in the unfavourable phase where the vacuum rf field is retarding. Second, the collective self-field of the bunch, always opposing emission near the surface, overcomes the vacuum rf field and limits emission even for a favourable

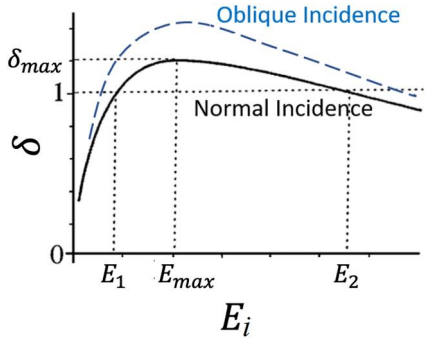

FIGURE 2 Schematic of the secondary electron yield (SEY) as a function of primary electron impact energy [6].

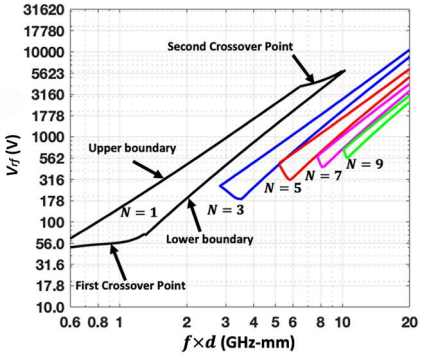

FIGURE 4 Multipactor susceptibility diagram for parallel-plate configuration with Cu electrodes obtained analytically for the first five modes, $N = 1, 3, 5, 7$ and 9 with emission energy, $V_0 = \frac{1}{2}mv_0^2 = 2$eV.

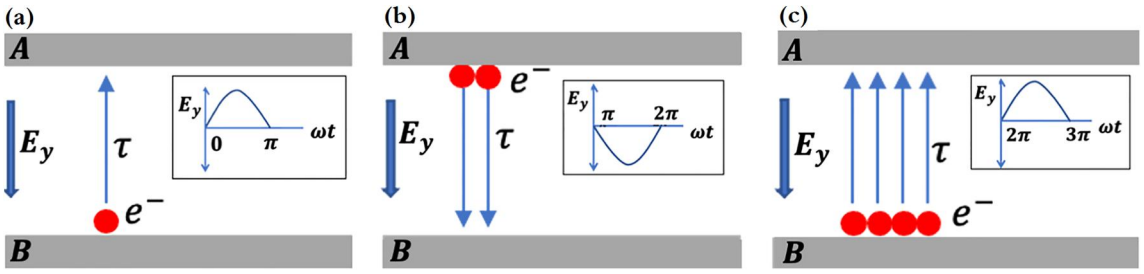

FIGURE 3 Multipactor discharge with an electric field oscillating between two metal electrodes A and B [25]. (a) $\omega t = 0 \rightarrow \pi$, (b) $\omega t = \pi \rightarrow 2\pi$, (c) $\omega t = 2\pi \rightarrow 3\pi$. Upon each electron impact, secondary electrons are emitted from the surface, multiplying the total number of electrons at each half cycle.

vacuum rf phase. These saturation effects, with the added effect of finite electron inertia, were shown computationally by Gopinath [86].

2.3 | Single surface multipactor

Single surface multipactor is of particular interest to the microwave community due to its severe adverse effects that can eventually lead to dielectric window failure. The physics of this phenomenon is different from that of the two surface multipactor and has led to a separate branch of multipactor research. Studies on single surface multipactor are relatively scarce in early literature. It was not until 1961 that the first theoretical treatment of single surface multipactor was introduced by Priest and Talcott [20]. In the late 1990's Kishek *et al.* expanded on that theory and conducted a comprehensive study [6] on this topic. In the following we present some basic properties of single surface multipactor, that is, the electron dynamics, susceptibility, and time-dependent physics.

Figure 5 shows the schematic of single surface multipactor discharge. An electric field $E_y = E_{rf}\sin(\omega t + \theta)$ is applied parallel to the surface along the y-direction. The multipactor electrons are subjected to forces imposed by this parallel electric field and the normal electric field E_x originating from the residual charge on the dielectric acting along the x-direction (Figure 5). The flight trajectory of a multipactor electron is governed by the force law,

$$m\frac{\partial \vec{v}}{\partial t} = -e\left[\hat{y}E_{rf}\sin(\omega t + \theta) + \hat{x}E_x\right]. \tag{7}$$

Having gained energy from the rf field during the flight, the electron strikes the surface with much larger energy, and therefore, induces the emission of secondary electrons [9–11]. These secondaries also leave the surface and strike back at a later time, gaining energy in the process. If the conditions are such that there is a net gain in the number of electrons, eventually a large amount of energy gained from the rf electric field will be deposited on the surface, possibly leading to surface damage or gas desorption that can lead to breakdown. It is important to note that, the transit time of the electron is short compared to an rf period. The transit time (τ_{trans}) as well as the energy of the electron impacting the surface (with components ϵ_x and ϵ_y, in directions normal and parallel to the surface, respectively) can be obtained from Equation (7) as follows, [6, 58, 61]

$$\tau_{trans} = 2mv_0\sin\phi/eE_x, \tag{8}$$

$$\epsilon_x = \frac{1}{2}m(v_0\sin\phi)^2, \tag{9}$$

$$\epsilon_y = \frac{1}{2m}(eE_{rf}/\omega)^2\left[\cos(\omega\tau_{trans}+\theta) - \cos\theta + \frac{mv_0\cos\phi}{eE_{rf}/\omega}\right]^2. \tag{10}$$

In their pioneering article in 1998 [6], Kishek and Lau presented the single surface multipactor susceptibility curves (shown in Figure 6a) as an efficient way to indicate the range of rf voltage (and power) over which an rf window may be susceptible to multipactor. The susceptibility curve can be obtained from simulation schemes such as single macroparticle [6, 43, 84] or multiparticle [60, 87] Monte Carlo (MC) simulations as well as PIC simulations [61, 88] and can be explained by a simple analytic theory proposed by Kishek and Lau [6]. If the design parameters lie within the multipactor boundaries of the susceptibility curve (representing a positive charge growth rate), then multipactor is possible and the design needs to be modified to mitigate multipactor.

Kim and Verboncoeur showed [61] that at the ac saturation for a given rf amplitude which occurs at the lower susceptibility boundary, the normal surface charging field (E_x) reaches a time-averaged saturation value and the temporal relationship between the fields normal and parallel to the surface traces a closed Lissajous curve [60, 88]. In addition, for a single-frequency rf electric field, the temporal profile of the normal electric field (E_x) oscillates at twice the rf frequency in the ac saturation state, as shown in Figure 6b.

Although classical single surface multipactor studies have almost exclusively focussed on conditions where a component of the rf field exists parallel to surface, it is noteworthy that a

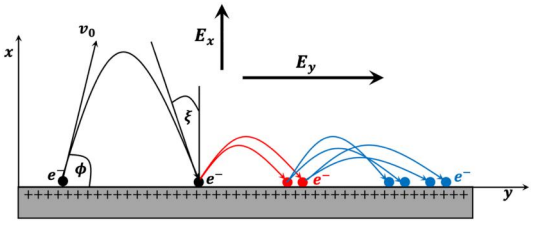

FIGURE 5 Schematic of the single surface multipactor discharge in a normal electric field (E_x) and a parallel electric field (E_y). v_0 and ϕ denote respectively the random emission velocity and angle of an electron emitted from the surface while ξ denotes the impact angle of the primary electron.

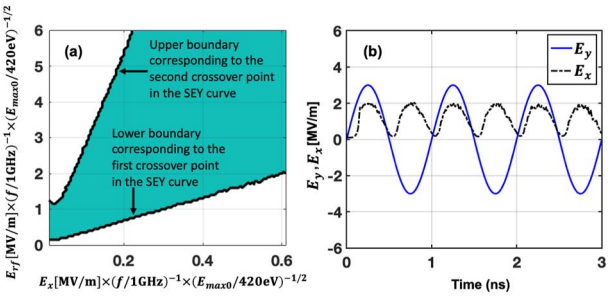

FIGURE 6 (a) Single surface multipactor susceptibility boundaries (cyan regions are subject to multipactor susceptibility) from Monte Carlo simulation in the (E_x, E_{rf}) plane (b) Instantaneous rf electric field, E_y (solid blue lines) and normal electric field, E_x (broken black lines) at the saturation state for $E_{rf} = 3$ MV/m. For both (a) and (b) Vaughan's SEY model parameters $\delta_{max0} = 3$, $E_{max0} = 420$ eV, $E_{0m}/E_{max0} = 0.005$ are used where δ_{max0} is the maximum secondary electron yield occurring at impact energy E_{max0}, and $2E_{0m}$ is the average emission energy of secondary electrons.

novel extension of rf breakdown susceptibility theory to the DC regime have also been formulated [27] by M.T.P. Alden.

2.4 | Multipactor in coaxial lines and complex geometries

Multipactor can occur in many complex geometries and devices. In the late 1960s Richard Woo experimentally determined multipactor susceptibility (Figure 7b) on a coaxial geometry (Figure 7a) [89, 90] and proposed a similarity principle [91] of multipactor susceptibility for complex geometries relative to the parallel-plate geometry. In 2006, T.P. Graves revised [25] Woo's data by removing surface impurities through Argon glow discharge cleaning process and found that a higher energy distribution of particles exists for the coaxial geometry as compared to the parallel plate geometry with the same electrode spacing depending on the outer-to-inner radius ratio of the coaxial geometry and therefore coaxial geometries are more susceptible to multipactor.

Developing an analytic theory of coaxial multipactor proved to be quite challenging due to the absence of a fully analytic solution for the electron trajectory [24, 72, 92]. In 2007, Udiljak *et al.* proposed [92] an useful approximate solution for the electron trajectory and showed that when the inner radius (a) of a cylindrical coaxial transmission line is of the order of the outer one (b), the multipactor properties are very similar to those of the parallel-plate geometry. However, when the inner radius is less than a certain threshold value [92], single-surface multipactor becomes possible. In addition, for certain radii ratios (b/a), both two-surface and single-surface multipactor can exist. These predictions were confirmed [93] by Semenov *et al.* through PIC simulations.

More recently, Siddiqi and Kishek [94] offered a predictive model for the onset of multipactor in a coaxial geometry based on chaos theory. The nonstationary statistical approach by Lin et al. [54] may be noted in this context. Space-charge effects in coaxial multipactor have also been studied analytically by Sorolla *et al* [95]. It is notable that in recent times we observe an increasing reliance on software tools such as CST [71, 72, 96, 97] and Spark-3D [69] for multipactor simulation in complex geometries, such as the cylindrical and elliptical coaxial lines, rf cavities, tapered waveguides, etc.

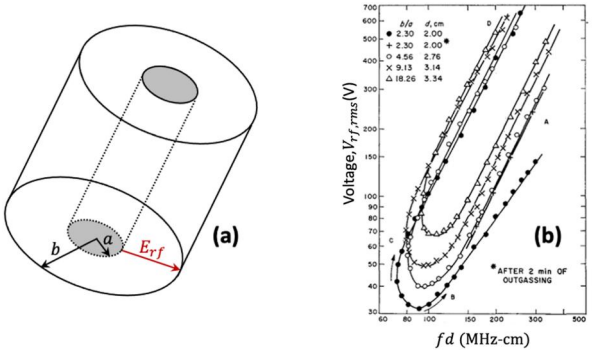

FIGURE 7 (a) Schematic of a coaxial geometry with inner radius, a, outer radius, b, and axial rf electric field, E_{rf}. (b) Multipactor susceptibility for coaxial electrodes with varying values of b/a [89].

3 | MULTIPACTOR MITIGATION

3.1 | General approaches

Over the years, multipactor mitigation has been a major focus of multipactor studies. A number of mitigation strategies have been adopted in various applications which can be roughly categorised into two approaches [84].

The first approach is mitigation by engineering the device susceptible to multipactor which can be further categorised into three methods: surface coating, surface conditioning, and geometric modification. Surface coating with low SEY materials is one of the earliest methods adopted for multipactor mitigation [98]. D. C. Joy provided [99] a large database of materials' SEY which has been very useful in this respect. Surface conditioning, commonly known as beam scrubbing [18, 19] in the particle accelerator community, uses a beam to induce multipactor and irradiate the surface with energetic electrons. These electrons scrub the surface by electron stimulated desorption (ESD) and surface graphitisation [26] to reduce further multipactor susceptibility. Geometric modification can be useful in two ways. Firstly, artificially roughened or porous surfaces can be introduced to reduce the SEY [8, 100, 101]. Secondly, device geometric modification can be employed to alter the trajectories of electrons so as to mitigate multipactor at frequencies of interest [102, 103].

The second approach of mitigation is by modifying the electric or magnetic fields in the devices. A. Valfells *et al.* showed [45] that a large external magnetic field perpendicular to the rf electric field and to the normal electric field can significantly reduce multipactor on a single dielectric surface. C. Chang *et al.* demonstrated [104, 105] that high-power microwave (HPM) dielectric multipactor can be suppressed by utilising external resonant magnetic field. O. A. Ivanov *et al.* demonstrated [106] in their experimental study that an external dc bias repulsing the charges from a single dielectric (quartz) surface can mitigate multipactor. In 2011, Chang *et al.* summarised recent theoretical and experimental progress on improving HPM multipactor and breakdown threshold [107]. Recently, instead of applying external electric or magnetic fields, there have been efforts to use multi-frequency or non-sinusoidal waveforms of the rf fields to mitigate multipactor [62, 108].

3.2 | Recent advances in device and surface engineering

In the past few decades, significant advances have been made in surface fabrication technology, enabling more advanced multipactor mitigation techniques to be employed. In late 2010s, it was observed that a deeply roughened (in millimetre [109] and nanometre [110] scale) metal surface exhibits

significant SEY suppression [111]. Artificially grooved surface geometry is also found to mitigate dielectric surface flashover [112, 113]. Pivi *et al.* theoretically explained [114] the effect of a roughened surface on the millimetre scale. In 2013, Ye *et al.* showed that the SEY of a roughened surface is affected significantly by the aspect ratio of the pores and the surface porosity of the metal plate [115]. Sattler *et al.* proposed an analytical model [116] to explain such dependence.

In the simple analytical model, Sattler *et al.* approximated a three-dimensional cylindrical pore as a two-dimensional rectangular well and estimated the effective surface SEY as [116],

$$\delta_{effective} = \delta_{flat}(1-\rho) + \left(\delta_{pore-bottom}\overline{P}_{escape-2D}\right)\rho \qquad (11)$$

where δ_{flat} is the SEY of the flat surface, $\delta_{pore-bottom}$ is the SEY of the bottom surface of the pore, ρ is the porosity of the surface given by the ratio of the pore surface area to the total surface area, and $\overline{P}_{escape-2D}$ is the mean escape probability of the first generation of secondary electron from the pore when a primary electron is normally incident at a random location of its bottom surface which is a function of the pore radius (R), pore height (H), and the distance from the pore centre to the emission site (r) (Figure 8c).

Later, Iqbal *et al.* found [117] that Sattler's analytical model, while reasonably accurate for surfaces with micropores of small aspect ratio ($A_R = \frac{H}{2R} < 0.55$), underestimates (Figure 8d) the effective surface SEY for micropores with a large aspect ratio ($A_R > 3$) due to the limitation that it only accounts for the first generation of secondary electrons generated inside the rectangular well. Iqbal *et al.* proposed [117, 118] an alternate Monte Carlo simulation scheme that takes into account all generations of secondary electrons generated inside a well and gives a more precise estimation of the mean escape probability of secondary electrons from a pore, and therefore, predicts the effective surface SEY more accurately (Figure 8d). In 2022, through an experimental study, Mirmozafari *et al.* demonstrated significant mitigation of two-surface multipactor [119] with surfaces consisting of through-pores (Figure 9a). The experimentally measured multipactor susceptibility diagram is in good agreement with model predictions using the SEY modelling of porous surfaces of Iqbal *et al.* [117] (Figure 9b).

In recent times, dielectric loaded microwave components have drawn significant interest because of their high Q-value and miniaturisation [121, 122]. Zhai *et al.* showed [121] that with a finite amount of initial charge on the dielectric surface, the multipactor threshold voltage initially increases and then declines with the increase of the initial surface charge density, σ. The decline of the threshold voltage results from an increase of the effective single surface impacts. Therefore, the electrostatic field produced by the initial charge on the dielectric surface can effectively reduce the risk of dielectric multipactor. It is also found [122] that pre-deposited positive charge on the dielectric surface can result in a lower multipactor strength at saturation.

Advanced surface coatings have also been developed to mitigate multipactor in recent years. Amorphous Carbon (a-C) coating (Figure 10a) has been found to be an excellent SEY mitigation scheme (Figure 10b) at the Large Hadron Collider (LHC) particle accelerator [123]. In the Fermilab main injector, diamond-like Carbon coating (DLC) has been found to mitigate multipactor to roughly 2% of that measured in the uncoated stainless steel beampipe [124]. In addition, significant SEY suppression (of almost up to 50% in [125]) has been

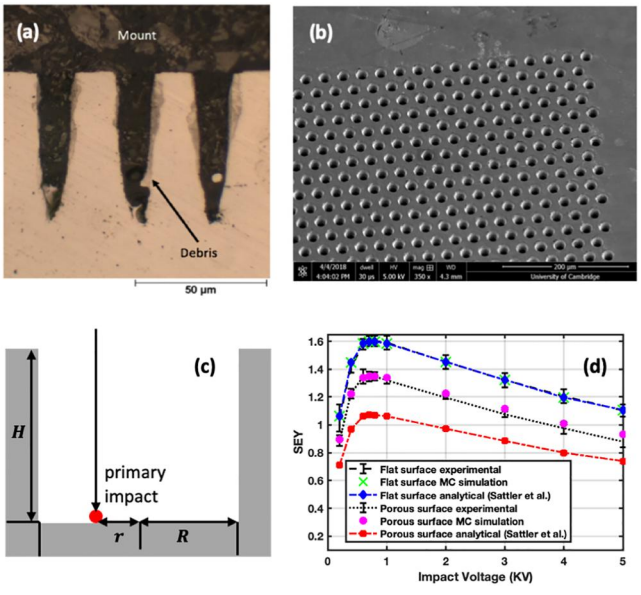

FIGURE 8 (a) Optical image of the cross-sectioned laser-drilled porous stainless steel surface sample with porosity, $\rho = 0.40$ and aspect ratio, $A_R = 3.02$. (b) SEM image of the same sample with magnification ×350. Both (a) and (b) are obtained before Au-coating [117]. (c) The 2D rectangular well geometry assumed in the analytical [116] and the Monte Carlo [117] models. (d) Comparison of the predicted SEY curves for normal incidence of primary electrons from the analytical model [116] and the MC simulation results [117] with the measured SEY curves [117] for the flat gold surface as well as the porous surface sample in (a)-(b) after Au-coating. Note that in (d), the predicted SEY curves from the analytical model as well as the MC simulation results are overlaid with the measured SEY curve for the flat surface.

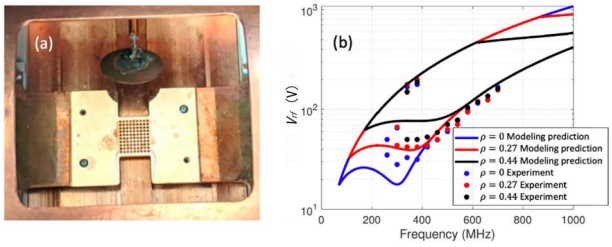

FIGURE 9 (a) The top view of the fabricated microstripline sections [119] with through-hole porosity, $\rho = 0.44$. (b) Two-surface multipactor susceptibility charts corresponding to $d = 3$ mm gap for different through-hole porosities [119]. Solid lines show the predicted susceptibility charts using a semi-analytic model [120] that employs porous surface SEY predictions from MC simulations of Iqbal *et al.* [117]. The dots represent the experimentally measured multipactor susceptibility boundaries. It is noteworthy that multipactor susceptibility region shrinks with increasing porosity (ρ) and with $\rho = 0.66$, the model predicts total suppression of the multipactor which agrees with the experimental measurements; therefore, the susceptibility region for $\rho = 0.66$ is absent in the figure.

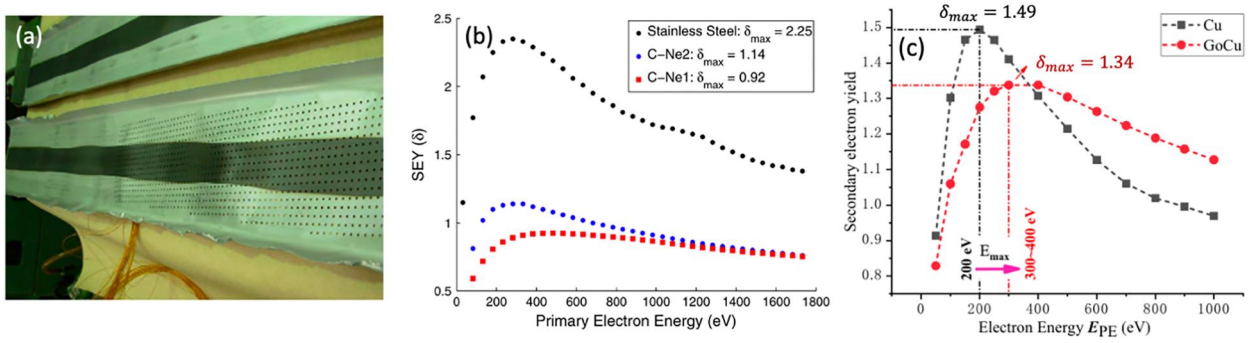

FIGURE 10 (a) Amorphous Carbon (a–c) coated (stripe region) liners used in the CERN Super Proton Synchrotron (SPS) [123]. (b) Comparison of the SEY of stainless steel and a–c coatings [123]; C-Ne1 represents coating of a–c as received and C-Ne2 represents coating of a–c aged in air for 2 weeks. (c) Secondary electron yield of Cu (black square dashed curve) and Graphene on Cu (red circle dashed curve) [128].

reported with graphene coated copper [126–128]. In 2017, Wu *et al.* proposed a simple fabrication process of porous Ag/TiO_2/Au coating [129] to combine a roughened structure with a low SEY material coated surface and obtained a greater SEY reduction with the combined approach than any of the techniques could obtain separately.

3.3 | Recent advances in waveform engineering

It is important to note that although the processes discussed above can be effective for multipactor mitigation in future devices, components already in use in various applications often cannot benefit from these treatments. For example, replacement of existing microwave components in satellites suffering degraded system performance and facing the risk of damage due to multipactor is not possible [130]. Moreover, system geometries may have engineering constraints or may be fixed by the necessary boundary conditions as in a waveguide, and other methods must be employed to prevent multipactor. To address this limitation, great emphasis has been put on multipactor mitigation techniques that modify the electric or magnetic fields in recent years.

It has been found that specific configurations of the two-frequency rf operation can reduce multipactor strength in both single-surface [60] and two-surface [131, 132] geometries compared to single frequency rf operation. In the single surface geometry, the modulation of the rf envelop due to the second carrier mode results in a lower instantaneous normal electric field (shown in the red circled region of the broken black curve in Figure 11a) for a longer duration during an rf period, which corresponds to a lower multipactor strength compared to Figure 6b [60]. The corresponding lissajous curve (Figure 11b) describing the temporal relationship between the rf electric field and the normal electric field consists of two small loops (shown in the red circled region in Figure 11b) representing the lower instantaneous normal electric field value as well as two large loops. It is found [87] that despite the existence of these large loops, the significant amount of time spent by the electric fields in the two small loops results in a lower time averaged

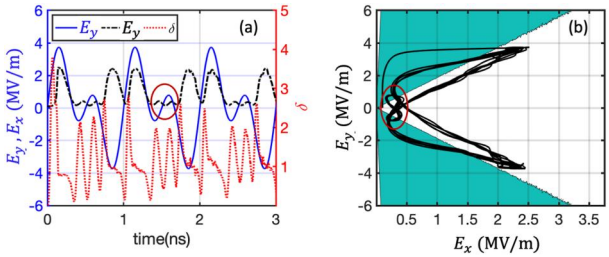

FIGURE 11 (a) Instantaneous rf electric field, E_y (solid blue line) and normal electric field, E_x (broken black line), and secondary electron yield δ (dotted red line) for two-frequency rf field, $E_y = E_{rf}\sin(\omega t + \theta) + \beta E_{rf}\sin(n(\omega t + \theta) + \gamma)$, [60] with frequency ratio $n = 2$, initial relative phase of the second carrier frequency, $\gamma = \pi/2$, and relative strength of the second carrier frequency $\beta = 1$, at the saturation state for rf carrier amplitude, $E_{rf} = 3/\sqrt{2}$ MV/m, and frequency of the fundamental carrier mode, $f_{rf} = 1$ GHz. (b)The corresponding plot of trajectories of the electric field $[E_x(t), E_y(t)]$ [60]. The shaded cyan region is the multipactor susceptibility region obtained by applying constant electric field, $E_{y,dc}$, parallel to the surface [60, 61].

multipactor strength with two frequency rf operation compared to that with the single frequency rf operation. In the two-surface geometry, similar modulation of the rf envelop along with space charge effects (to be further discussed in Section 4) lead to disruption of the resonant electron motion, resulting in multipactor mitigation [131].

Wen *et al.* found [108, 133] that non-sinusoidal gaussian type rf waveshapes can mitigate multipactor strength in the single surface geometry by orders of magnitude compared to a single-frequency sinusoidal rf waveshape with the same input rf power. This happens because as the width of the gaussian pulse decreases for a fixed input rf power, the longer decay time between the gaussian field peaks eliminates most free electrons [133]. Figure 12b shows the multipactor susceptibility chart corresponding to a gaussian type rf field [108]. We observe that for a fixed input rf power, $\overline{P}_{rf}$, the saturation value of the normal electric field E_x (at the lower susceptibility boundary) with the gaussian type rf field (Figure 12b) is significantly smaller than that with the sinusoidal rf field (Figure 6a). In Figure 12c, the time-averaged ratio of the multipactor power (that is, the power deposited on the surface through multipactor discharge , $\overline{P}_m$) to

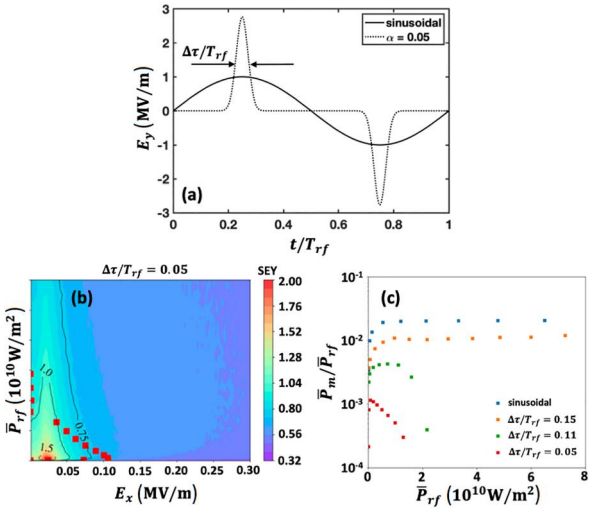

FIGURE 12 (a) The sinusoidal and Gaussian-type transverse rf electric fields for the same input rf power. (b) Multipactor susceptibility for Gaussian-type transverse rf electric fields with Gaussian width $\Delta\tau/T_{rf} = 0.05$ in the plane of input rf power, $\overline{P}_{rf}$, and normal electric field, E_x [108]. The contour plot with SEY shown in the colorbar is obtained from multiparticle Monte Carlo simulation [60] and the red points represent the time-averaged E_x of the time-varying restoring field at the ac saturation state representing the multipactor strength for various $\overline{P}_{rf}$ from self-consistent PIC simulation [61, 133]. (c) The time-averaged multipactor and rf power ratio $\overline{P}_m/\overline{P}_{rf}$ as a function of $\overline{P}_{rf}$ for sinusoidal and Gaussian waveforms with different $\Delta\tau/T_{rf}$ from PIC simulations [108].

the rf power $(\overline{P}_{rf})$ is shown. We observe that the fraction of rf power consumed by multipactor discharges decreases monotonously from a few percent to the order of 10^{-3} (even 10^{-4}) when the waveform shape is adjusted from a conventional sinusoidal function to a narrower Gaussian-type waveform. We also observe that multipactor is completely suppressed for a gaussian width of $\Delta\tau/T_{rf} = 0.05$ for $\overline{P}_{rf} > 3 \times 10^{10}$ W/m^2.

4 | RECENT ADVANCES IN MULTIPACTOR PREDICTION AND PHYSICS

4.1 | Novel multipactor prediction methods for multicarrier RF operation

A great emphasis has been put into the prediction and characterisation of multipactor under multicarrier rf operation since multicarrier operation becomes increasingly important in diverse modern applications. Multipactor prediction for multicarrier signals in a parallel plate geometry had previously been widely covered by the empirical "20-gap-crossing rule (20GCR)", proposed in the 2003 version of the multipactor standard published by the European Cooperation for Space Standardisation (ECSS) [134]. However, the latest 2020 version of the ECSS multipactor standard [135], presents two alternate methods for multipactor prediction with multicarrier signals: the pulsed method and the envelope sweep (ES) method. In the empirical pulsed method, a multicarrier signal envelop is approximated by a rectangular pulse. Empirical equations [136] are used to calculate the net electron growth rate over a complete period of the rectangular pulse representing the multicarrier signal. A global optimization method is employed to determine the worst case phase combinations of the multicarrier operation, where the cost function is defined as the carrier amplitude leading to multipactor breakdown for each phase combination. The envelope sweep method makes the global optimization scheme more efficient by reducing the solution domain, in order to enable the use of 3D numerical software in reasonable computation times. It is important, however, to note that both these prediction methods are largely empirical. The physics based understanding of the multipactor under multicarrier operation is still limited. In this regard, a series of recent publications [59, 60, 87, 131] on two-frequency rf field induced two surface multipactor are noteworthy, which have shed light on some important new physics that can be useful in developing a more comprehensive understanding of multipactor under multicarrier operation.

4.2 | Mixed multipactor modes for two-carrier RF operation

According to Vaughan's classical resonance theory of the two surface multipactor [2], under single multipactor modes (i.e., point m in Figure 13a), a multipacting electron takes a fixed time (τ_{total}) to complete a round trip between two parallel surfaces (let us denote the two surfaces by A and B for ease of the following discussion) and it also takes fixed times to traverse the gap distance once during this round trip (Figure 13b) in the forward path ($\tau_{A\to B}$) and the return path ($\tau_{B\to A}$), that is, $\tau_{A\to B} = \tau_{B\to A}$. However, under two-frequency rf operation, novel multipactor modes have been observed [131] (i.e., point n in Figure 13a) where an electron takes a fixed time to complete each round trip, however, the times required by the electron to traverse the gap distance once during this round trip are different in the forward path and the return path (Figure 13c), that is, $\tau_{A\to B} \neq \tau_{B\to A}$ and yet $\tau_{A\to B} + \tau_{B\to A} = \tau_{total}$, where τ_{total} is a constant.

4.3 | Space charge effects

The effects of space charge on multipactor saturation have been extensively studied both analytically [2, 44, 95, 137] and computationally [44, 138]. In recent years, advanced computing capabilities and software (i.e., XPDP1, XOOPIC, CST, FEST3D, MEST, etc.) have made it possible to take space charge effects into account in complex multipacting simulations. The role of space charge on multipactor susceptibility, which was largely unexplored until late 2000s, has been given particular attention in many recent studies [68, 131, 139]. In 2017, Romanov *et al.* showed [96] with CST PIC simulations that the first order multipactor bands with space charge effect are shifted towards higher field levels, and they are narrower than the ones simulated without space charge. They attributed these observations to a lower impact energy of particles colliding with the wall.

Indeed, the effect of space charge on multipactor dynamics and multipactor susceptibility largely depends on the initial conditions for multipactor onset. If multipactor growth starts from a very small number of particles, that is, the initial seed current density (J_{seed}) is very low, space-charge will have negligible effect on multipactor susceptibility as shown in Figure 14a. However, in situations with high initial seed current density (Figure 14b), space-charge can cause a narrowing of the susceptibility bands by increasing the multipactor threshold. Iqbal et al. attributed [131] this shrinkage of susceptibility bands to space-charge effects such as the virtual cathode effect, the disruption of resonant electron motion, and the reduction of electron impact energy resulting in a low average SEY. Figure 14c shows that when space charge is turned on in the CST simulation, the particle growth rate decreases with the increase of the initial seed current density, J_{seed}, and the minimum value of J_{seed} that can completely suppress multipactor at $\left(V_{rf}\ (\mathrm{V}), f(\mathrm{GHz}), d\ (\mathrm{mm})\right) \sim (369.58, 1, 3.1115)$ is, $J_{seed,min} \geq 6.30 \times 10^{8}\ \mathrm{A/m^2}$. Such initial seed current level may result from emission mechanisms such as field emission from local surface imperfections (e.g. defects, grain boundaries, surface roughness, contaminants, adsorbates, etc) or certain geometric configurations (e.g. sharp corners, edges, triple points, etc) to release a short burst of large number of electrons. For instance, Fowler-Nordheim field emission [140–142] can result in a current burst of $I_{seed} \geq 0.0630$ A at $\left(V_{rf}\ (\mathrm{V}), d\ (\mathrm{mm})\right) \sim (369.58, 3.1115)$ from a copper surface for a local field enhancement factor of $\beta_{local} \geq 6 \times 10^{4}$, if one assumes an emission area of $10^{-10}\ \mathrm{m^2}$. Such a current level is even more accessible when one uses photon excitation, for example, UV seeding, where it is known that the combined dc/rf field and photons can yield a few orders of magnitude larger emission current than either field emission or photoemission alone [143–145].

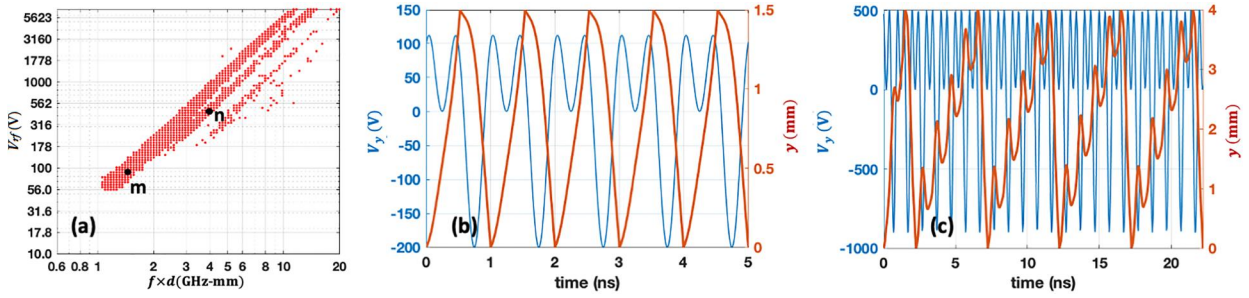

FIGURE 13 (a) Multipactor susceptibility chart in the $\left(V_{rf}, fd\right)$ space calculated from MC simulation [131] for two-frequency rf voltage, $V_y = V_{rf}\sin(\omega t + \theta) + \beta V_{rf}\sin(n(\omega t + \theta) + \gamma)$, with frequency ratio $n = 2$, initial relative phase of the second carrier frequency, $\gamma = \pi/2$, and relative strength of the second carrier frequency $\beta = 1$. (b)–(c) Instantaneous rf voltage (blue lines) and the corresponding macroparticle trajectories (red lines) [131] for (b) $V_{rf} = 100$ V; $fd = 1.5$ GHz·mm, and (c) $V_{rf} = 800$ V; $fd = 10$ GHz·mm. For both the cases, we use fundamental rf frequency, $f = 1$ GHz; and the variation of fd is obtained by varying the gap distance, d. Plots (b) and (c) correspond to the points m and n in the susceptibility chart in (a), respectively.

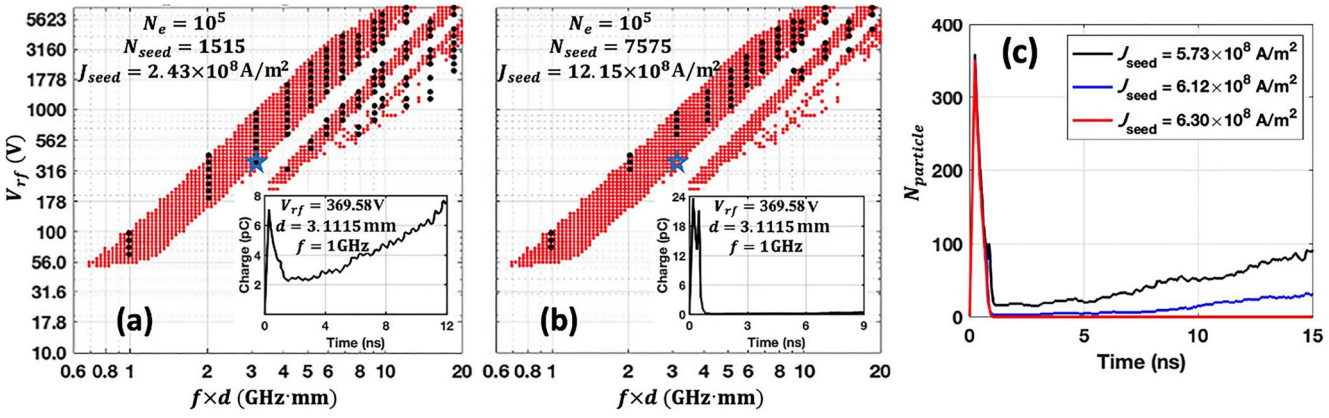

FIGURE 14 (a)-(b): Multipactor susceptibility charts in the $\left(V_{rf}, fd\right)$ space calculated from MC simulation (red dots) without the space-charge effect along with CST simulation (black dots) with space charge effect for number of seed particles (a) $N_{seed} = 1515$ [131] and (b) $N_{seed} = 7575$. For (a)-(b), the number of electrons in each computer particle, $N_e = 10^5$, emission area, $S_{eff} = 10^{-10}\ \mathrm{m^2}$, and emission time, $t_{emission} = 1$ ns are used. The corresponding charge growth at $V_{rf} = 369.58$ V and $d = 3.1115$ mm (marked with blue stars in the susceptibility charts of Figs. (a)-(b)) is shown in inset of each figure. Note that for the higher initial seed current in (b), the susceptibility bands with space charge effect are significantly narrower. (c) Number of particles versus time for three different initial seed currents, $J_{seed} = 5.73 \times 10^{8}\ \mathrm{A/m^2}$ (black curve), $J_{seed} = 6.12 \times 10^{8}\ \mathrm{A/m^2}$ (blue curve), and $J_{seed} = 6.30 \times 10^{8}\ \mathrm{A/m^2}$ (red curve) at $V_{rf} = 369.58$ V and $d = 3.1115$ mm.

4.4 | Controlling multipactor particle trajectories

In 2017, Rice *et al.* examined the feasibility [132] of employing a harmonic mode of the fundamental carrier frequency of a multi-frequency rf field to control the transverse deflection present in a multipactor current in the two-surface geometry. The results showed that for the second, third, and fourth harmonics of the fundamental carrier mode, controlling the migration of multipactor impact points within the geometry is possible, typically when the harmonic mode magnetic field is much stronger than the fundamental mode magnetic field. It has been later found by Iqbal *et al.* [60] that, in the single surface geometry as well, a mean horizontal displacement of the multipacting electrons over a complete rf period can be obtained with a two-frequency driving rf field. As shown in Figure 15, the asymmetry of the instantaneous rf electric field (blue curve in Figure 15a) causes the mean horizontal (along the y-direction in Figure 15b) excursion of multipacting electrons. The excursion can be controlled by tuning the relative phase and strength of the second carrier mode with respect to the fundamental carrier mode [60]. The controllability of multipacting particle trajectories can be of particular interest to rf system designers and engineers in applications such as cleaning a given location in a structure to reduce further susceptibility to multipactor, distributing the thermal load from multipactor to reduce gas desorption or local loss of superconductivity, or for directing multipacting electrons to a specific desirable location in the geometry [62].

4.5 | Single-surface multipactor at oblique rf electric field

In the literature, most studies relevant to single-surface multipactor discharges focus on the scenario where the rf electric field is tangential to the surface and the restoring electric field is normal to the surface as discussed above. However, in reality, there may exist an oblique angle between the rf electric field and the surface, θ (see Figure 16a). The susceptibility of the multipactor discharge was found to be greatest when the rf electric field is nearly parallel to the surface, and significantly reduced for θ greater than 10° ($\pi/18$) [45]. Wen et al conducted self-consistent PIC simulation [146] and the results, as shown in Figure 16b, indicates that the multipactor discharge strength represented by the residual surface charge density is significantly decreased when θ increases for commonly used carrier frequency and strength of rf electric field in communication. In addition, the primary electrons flying in space are forced into a few branches in the phase space of velocity and position, that is, the electrons have a few groups of velocities at a fixed position due to the increased electron hop time in the phase when the normal component of the oblique rf electric field enhance the hop. Clearly, the perpendicular component reinforces or reduces the restoring electric field, and thus increases or decreases the secondary electron emission in half of the rf period. At some special resonant conditions, a multipactor discharge similar to two-surface multipactor may occur, more details could be found in [147].

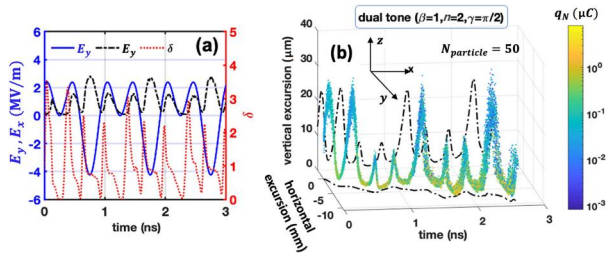

FIGURE 15 (a) Instantaneous rf electric field, E_y (solid blue line) and normal electric field, E_x (broken black line), and secondary electron yield δ (dotted red line) for two-frequency rf field, $E_y = E_{rf}\sin(\omega t + \theta) + \beta E_{rf}\sin(n(\omega t + \theta) + \gamma)$ [62], with frequency ratio $n = 2$, initial relative phase of the second carrier frequency, $\gamma = \pi/2$, and relative strength of the second carrier frequency $\beta = 1$, at the saturation state for rf frequency of the fundamental carrier mode, $f_{rf} = 1$ GHz. (b) Horizontal (along the dielectric surface) and vertical (normal to the surface) excursions of 50 multipacting macroparticles with respect to time, for two-frequency rf electric field with $f_{rf} = 1$ GHz, $\theta = 0$, $\beta = 1$, $n = 2$, and $\gamma = \pi/2$ [62].

4.6 | Frequency domain analysis

Frequency domain analysis of multipactor has been of particular interest to the scientific community during the past decade. In 2018, Zhang *et al.* [148] conducted a numerical study on this topic for the two surface geometry and diagnosed passive intermodulation (PIM) interference caused by multipaction for two-frequency as well as four-frequency rf operations. In 2021, Yang *et al.* [149] proposed an analytical method to evaluate the spectrum of rf noise caused by multicarrier multipactor discharge. They showed that in the first-order multipacting resonance $(N = 1)$, the odd harmonics $(f, 3f, 5f, ..., nf)$ of the rf field are generated (Figure 17a), where f denotes the greatest common divisor of the carrier frequencies and n is a positive odd integer. In the higher order multipacting resonance $N \geq 3$, the subharmonics are generated and the frequencies of the multipactor noise can be described by $2\pi nf/N$, where n is an odd integer (Figure 17b). They also

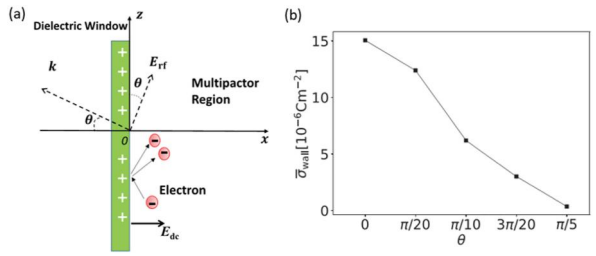

FIGURE 16 (a) Schematic of a single surface of multipactor with the electric field of the plane wave oscillating and propagating in x-z plane [146], k is the Poynting vector and θ is the oblique angle between k and surface normal. (b) time-averaged surface charge density at saturation state versus θ [146]. The carrier frequency and amplitude of rf electric field are 2.85 GHz and 3 MV/m, respectively.

observed that the magnitude of the multicarrier multipactor noise, including harmonics and subharmonics, decreases with increasing n (Figure 17b). Wong *et al.* showed [150] that harmonics of the driving rf voltage may be generated in the current of multipactor discharge through the charge orbits crowding and the phase-focussing mechanism [41]. Higher harmonic generation could be an important beneficial application of two-surface multipactor discharge.

In 2020, Iqbal *et al.* presented [151] a frequency-domain investigation of multipactor discharge in single dielectric surfaces. They observed that the amplitude spectrum of the normal electric field induced by a single-frequency rf field consists of pronounced peaks at even harmonics of the driving rf frequency (Figure 18a). For two-frequency rf operation, the normal electric field in the ac saturation state consists of frequency components at various intermodulation products (Figure 18b) of the driving rf carrier frequencies.

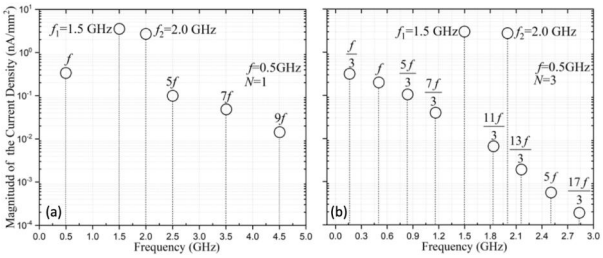

FIGURE 17 Frequency components of the (a) first and (b) third orders ($N = 1, N = 3$) two-surface multipactor discharge for two-frequency operation with carrier frequencies $f_1 = 1.5$ GHz, $f_2 = 2.0$ GHz [149]. The frequency for the multicarrier signal is the greatest common divisor of the carrier frequencies [48], that is, 0.5 GHz. Two conclusions are drawn from the calculated results: 1) both the harmonics $(f, 3f, 5f, \ldots)$ and subharmonics $(f/3, f, 5f/3, \ldots)$ decrease with frequency; 2) the third, fifth orders harmonics and seventh, eleventh, thirteenth orders subharmonics are close to the carrier frequencies; therefore, those frequencies should be treated carefully in engineering.

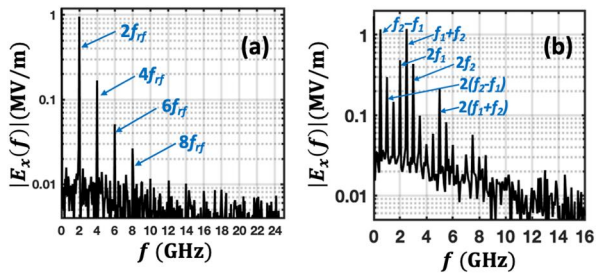

FIGURE 18 Amplitude spectrum of the normal electric field to a dielectric surface in the ac saturation state induced by (a) a single frequency rf field with amplitude, $E_{rf} = 3$MV/m, and frequency, $f_{rf} = 1$ GHz [151]. Pronounced spectral peaks are observed at even harmonics of the rf frequency. (b) a two-frequency rf field with individual carrier amplitude, $E_{rf} = 3$MV/m (with $\beta = 1$), and carrier frequencies, $f_1 = 1$ GHz, $f_2 = 1.5$ GHz [151]. Pronounced spectral peaks are observed at frequencies $(f_2 \pm f_1)$, $2f_{1,2}$, and $2(f_2 \pm f_1)$. For all cases, the heights of the spectral peaks are found to be independent of the rf frequencies [151] and proportional to the driving rf field amplitudes.

4.7 | Multipactor at different frequency operations

Figure 19 shows a comparison of parallel-plate metal multipactor susceptibility measured at different frequencies [25, 89, 152] in the L-band regime with the analytical susceptibility chart of Figure 4. As can be inferred from Eq. (6), Figure 19 shows that the measured multipactor threshold voltage scales as a function of $(fd)^2$ for different frequency operations. More recently, multipactor threshold measurements of high order (N = 17–19) have been reported [153] in the S-band (2.85 GHz) regime. In addition to metals, most commonly used dielectrics in space applications, namely, Alumina, Rexolite, Rogers RT5870, Rohacell, Teflon, and Ultem 1000, have also been characterised in the L-band and the S-band (1.3–3.97 GHz) regime (See Table VII and VII and Fig. 9 of [154] for detailed data) in terms of multipactor threshold voltage and power, in the parallel-plate configuration.

In the last couple of decades, application of high power microwave sources at subterahertz and terahertz frequencies [155–157] has become increasingly important for many applications including data communications [158], sensing [159], medical sciences, biology, and imaging [155, 160, 161]. Therefore, understanding multipacting behaviour at the high frequency regime has become pertinent. In 2010, Ivanov *et al.* experimentally studied [106] single surface multipactor mitigation with external dc bias at an operating frequency of 9.4 GHz which was the state of the art of multipacting experiments at high frequency at the time. This upper limit has recently been significantly improved. In 2019, Schaub *et al.* validated [7] the linear scaling of single surface multipactor thresholds up to the frequency of 110 GHz (Figure 20). They also found that rf power dissipated in the multipactor (i.e., the power loss due to surface multipactor), when the rf field acts parallel to the surface (i.e., in a dielectric window), is small and independent of rf intensity. On the other hand, power loss in a geometry where a strong rf field component exists

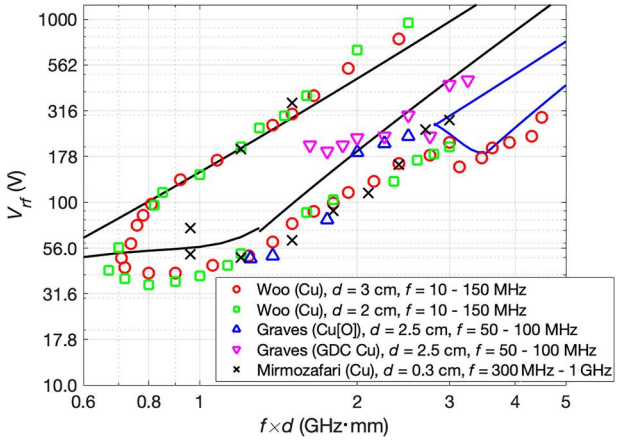

FIGURE 19 Measured parallel-plate metal multipactor susceptibility at frequencies from 100 MHz to 1 GHz for commercial Cu [25, 89, 152] and Argon glow discharge cleaned Cu (GDC Cu) [25] are compared with the analytical susceptibility chart (solid lines) of Figure 4.

perpendicular to the surface (i.e., in a dielectric loaded waveguide), grows linearly with the rf field and can lead to high losses within a small surface area.

4.8 | Signal quality degradation due to multipactor

The distortion of signal due to multipacting is a big concern in rf applications. Therefore, the prediction and quantification of such degradation is of great importance. Several theoretical models have been employed by researchers during the 1990s and 2000s in this regard. Kishek and Lau proposed [40] a simple time domain model to study the interaction between multipactor discharge and rf circuit. Nagesh *et al.* employed [13] the dyadic Green's function technique for computing the radiated electric field due to multipactor current in a coaxial geometry and found that a distortion in the rf field occurs within the gap due to multipactor. Later studies also showed [165–168] unwanted frequencies can be generated due to multipactor resulting in distortion of the rf signals.

In 2019, Wong *et al.* proposed an analytical model to quantify the effects of multipactor on the quality of the signal that propagates along a transmission line (TL) (Figure 21a). They demonstrated that regardless of geometry and signal drive, the error on the propagating rf signal due to multipactor has a magnitude roughly proportional to the multipactor current induced by the original signal. They also found that as multipacting takes place, the rf signal experiences both amplitude and phase modulation (see the I-Q plot in Figure 21b) and the perturbation amplitude due to multipactor is at most a single-digit percentage of the original transmission line signal for the chosen parameters.

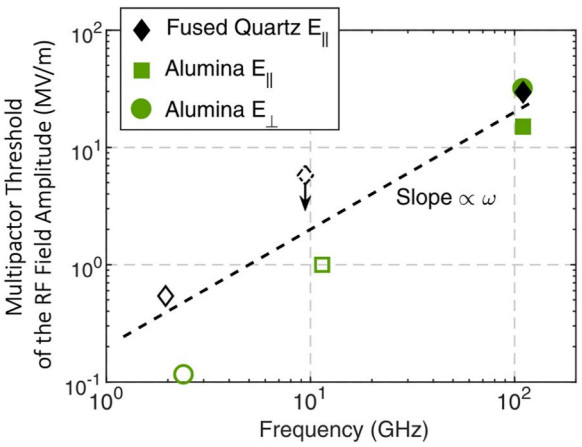

FIGURE 20 Dielectric multipactor thresholds [7] at frequencies from 2 to 11 GHz [106, 162–164] (hollow solid and dashed symbols) are compared with the data at 110 GHz (filled symbols). Data include parallel (to the surface) rf field geometry for fused quartz (diamonds) and alumina (squares) as well as perpendicular (to the surface) rf field geometry for alumina (circles). The dashed line is drawn to illustrate the theoretical linear dependence of threshold field on frequency and is not a fit to the data.

5 | MULTIPACTOR AND VOLUME BREAKDOWN

In the sections above, we have reviewed the multipactor physics in vacuum. However, in presence of neutral atoms or molecules near a dielectric surface or between two planar plates, the electron dynamics would be altered due to the elastic and inelastic electron-neutral momentum transfer, excitation and ionization events.

5.1 | Fundamentals

The investigation of volume breakdown phenomenon along a dielectric surface can be traced back to the early 1980s in a dc high-voltage system [169, 170], that was primarily in vacuum surrounded by cathode-insulator-anode. The volume breakdown, also known as surface flashover in early times, is generally initiated by the emission of electrons from the cathode triple junction (i.e. junction of vacuum, insulator, and metal). In order to understand the physics of flashover, a series of experiments and modelling attempts were conducted. Hegeler *et al.* [171] experimentally measured the current, luminosity, and soft X-ray emission via high-speed electrical and optical diagnostics with a resolution of 1 ns. It was found that both the current and luminosity increase linearly first, followed by an exponential increase. An increasing X-ray emission is also measured in the linear phase, but it ceases on the onset of exponential phase. The linear-stage current is strongly influenced by externally applied magnetic field, indicating the existence of flying free electrons above the surface [172], and meanwhile, the X-ray confirms the presence of high-energy electrons from the acceleration of high electric field in the early stage of flashover and it is from the bremsstrahlung radiation generated by impacting electrons [74]. Neuber *et al.* [173] observed the time-resolved spectroscopy of excited atomic hydrogen and ionic carbon that originally from water or

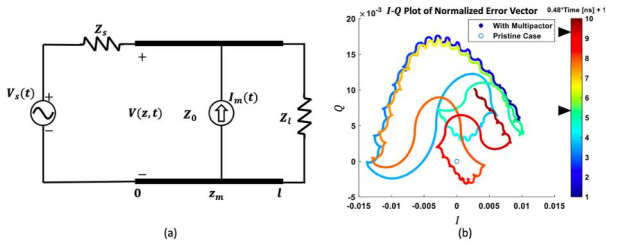

FIGURE 21 (a) Transmission line model to analyse the effects of multipactor on the quality of a signal [24]. (b) A parametric I-Q plot [24] of the normalised error due to single-surface multipactor in coaxial geometry, showing the temporal evolution of two components of the voltage waveform due only to multipactor (i.e., an "I (In-phase)" component (which is in phase with the original signal) and an orthogonal "Q (Quadrature)" component). At any point on the I-Q plot, the amplitude of the error introduced by multipactor is $\sqrt{I^2+Q^2}$ relative to the pristine case (the origin) and the phase of the error is the angle measured from the I-axis. In the calculation, the following parameters are used: $V_{s,max} = 2400$ V, $f = 3$ GHz, $z_m = 0.1$ m, $l = 1$ m, and $Z_0 = Z_l = Z_s = 41.56\ \Omega$ (see [24] for details).

impurities like carbon dioxide or carbon monoxide adsorbed on dielectric surfaces, indicating that an outgassing process is present due to the electrons bombarding the surface.

It was an important step to identify that the main process for breakdown is above the surface rather than the collision processes inside the material below the surface or within the adsorbed thin gas layer. The basic physical step-by-step picture identified by early experiments is as following: electrons from the cathode triple junction due to enhanced field emission are accelerated by the high transverse electric field and undergo multiple impacts along the surface, leading to an increased electron number during successive impacts, that is, secondary electron emission avalanche (or multipactor); meanwhile, the electron impacts trigger the desorption of gas that was adsorbed on the surface, and the desorbed atoms/molecules are excited to higher excitation states or ionised by energetic electron collisions, eventually a gaseous breakdown appears. The mechanisms above are found to be appliable to microwave surface breakdown if the microwave frequency is below 20 GHz where the typical hop time of electrons are much smaller than the microwave period [173].

Microwave volume breakdown was more comprehensively investigated after late 1990s [74]. In laboratory microwave systems, the downstream side of a dielectric layer can be vacuum or atmosphere, depending on the application. If the dielectric layer is a high power microwave window for signal emission, the downstream side is usually atmosphere or other natural environment. It was found in vacuum waveguides that the threshold for downstream breakdown is higher than the upstream (note that both upstream and downstream side breakdown starts from vacuum as the windows locates in a vacuum waveguide), because of the directed migration of the electrons along the microwave propagation direction under the action of $E_{rf} \times B_{rf}$ force of the microwave fields [74, 174].

Two-dimensional plasma filamentary arrays were first observed experimentally by Hidaka *et al.* [175] as shown in Figure 22a during high power microwave breakdown of air at atmospheric pressure near a dielectric surface. Each existing plasma filament was regularly spaced about one-quarter of microwave wavelength and elongated along the electric field direction. The plasma arrays propagate towards the microwave source. Later, the filamentation mechanism was explained by a theory constructed by Nam *et al.* [76] and Boeuf *et al.* [77], incorporating the microwave transmission, reflection, absorption, plasma diffusion and ionization. The electric field was reflected and scattered by the plasma filament having density high enough, and the electric field forms a peak value at one-quarter wavelength away from the reflective plasma at the first electric field peak as shown in Figure 22b. The maximum field induced a new ionization breakdown, finally leading to sequential plasma filament development and propagation. More comprehensive studies of experiments and modelling at different external conditions were also conducted, for example, the plasma arrays transform to a smeared-out array and finally to a diffuse plasma when the pressure decreases from atmosphere pressure to a few Torrs [176].

The wave reflection and damping are significant if the microwave pulse is long enough that plasma density increases to be very high ($f_{pe} \gtrsim f_{rf}$, where f_{pe} is the electron plasma frequency) and wave skin depth is short compared to the filament thickness, therefore, the plasma breakdown time is of importance. Krile *et al.* [177] conducted Monte Carlo simulations for effective tangential electric field amplitude as a function of ionization breakdown time in air and compared the simulations to experiments, showing that the lower electric field strength requires longer ionization time for breakdown as shown in Figure 23a.

Lau *et al.* derived a theoretical scaling law for discharge formation time via estimating the ionization rate at low- and high-pressure limits [178]. It shows the ionization breakdown time decreases first and then increases with a transition near 10Torr (see Figure 23b), this is because of the collision property where the ionization rate almost linearly increases in the low pressure range while the product of the ionization cross section and electron velocity is close to a constant for electrons with energy 100 eV to 2 keV. At higher pressure where the collision rate is very frequent, electrons lose energy via collisions rapidly, therefore fewer electrons exceed ionization threshold energy, leading to a longer breakdown time for higher pressure. The effect of the microwave frequency and electron energy distribution function was investigated via global model by Nam *et al.* [179, 180], and it was found that a Maxwellian assumption for electron energy distribution leads to a significantly underestimated ionization time due to inaccurate reaction rate coefficients. Theory and global modelling have to make certain assumptions and do not consider spatial

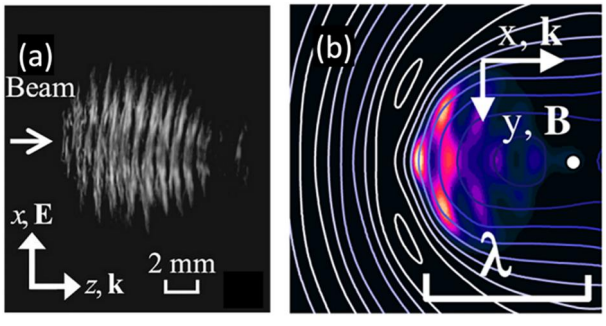

FIGURE 22 (a) Experimentally measured time-averaged volume breakdown plasma structure [175]; (b) The plasma filament from 2D modelling incorporating plasma diffusion, ionization and microwave propagation [77].

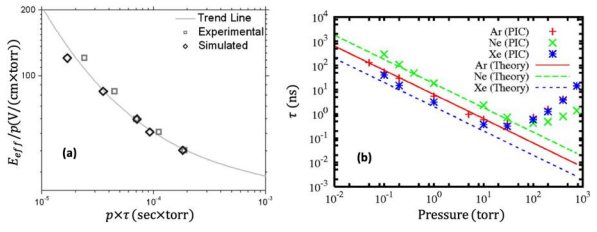

FIGURE 23 The breakdown time from (a) Monte Carlo simulation and experiments at atmosphere pressure [177]. (b) Theory and kinetic particle-in-cell simulations at various pressures from 10^{-2} to 760 Torr [178].

dependence of the properties. A more complete description for ionization breakdown processes involving plasma-surface interaction and volume ionization requires a particle-based kinetic simulation. Kim *et al.* [88] investigated the transition of window breakdown from single surface vacuum multipactor discharge to rf plasma in a wide range of pressure using PIC simulations. At low pressure the electron density peak locates near the surface, sustained by the electron multipactor process; at high pressure, the plasma density peak moves from the surface to space where the ion density equals to the electron density, and the electron energy has a Druyvesteyn distribution with significantly depressed high energy tail. The multipactor process can even be fully suppressed when the electron-neutral collision frequency is high enough that the electron impact energy on the surface is insufficient to kick off secondary electrons. A negative sheath can occur when the electron flux to the wall from the plasma region exceeds the creation rate of multipactor electrons, causing a reversal of surface charge which repels electrons, eliminating the multipactor. In addition, the electron density shows two peaks located on the surface and in space at intermediate pressure (~Torr), as shown in Figure 24, indicating that multipactor discharge and rf plasma coexist at least briefly.

5.2 | Recent advances

In recent years, more understanding about the volume breakdown process has been accumulated for high power microwave (HPM) transmission. The plasmas are generated within nanosecond time scale for high power microwave radiation through the dielectric/air interface separating the vacuum and air as discussed above. Neuber *et al.* [181] investigated the plasma relaxation time for microsecond HPM pulses at the MW level, that is, the lifetime of plasma due to losses via diffusion and volume chemical reactions in the pressure range from 10 to 600 Torr as the residual plasma can affect the next microwave pulse. The dominant electron loss mechanisms such as 3-body attachment for air, 2-body recombination for N_2, as well as the electron-temperature loss channel for Helium are revealed. The authors also experimentally confirmed that increasing the roughness or changing the profile of a dielectric surface, for example, grooving a flat surface to a corrugated shape, can increase the electric field strength, allowing for transmission of higher power [182]. In nanosecond time scale HPM breakdown, Chang *et al.* [75, 183] investigated the ultrafast discharge in air and observed a thin layer of intense light emission above the dielectric/air interface after the HPM pulse, and it is explained by the formation of a space-charge microwave sheath superimposed on the components of the electromagnetic wave normal to surface, that enhances the local field amplitude and therefore the ionization and excitation. The photoelectrons produced by photons are found to profoundly promote discharge and fast propagation in the air. On the vacuum/dielectric side, measurements of the time- and space-dependent optical emissions indicate that the multipactor and plasma also develop within a layer of several millimetres above the interface after the main microwave pulse, meanwhile, analysis and simulations reveal ionization concentrated in a desorbed gas layer with a pressure around hundreds of mTorr [184].

More recently, in order to investigate basic physics of the plasma breakdown dynamics in the early stages, Wen *et al.* [78, 79] conducted fully kinetic PIC simulations [88, 185, 186] for multipactor and plasma breakdown near a dielectric surface. The background gas pressure is fixed near hundreds of mTorr to make the simulations more general for plasma breakdown. A multilayer-structured discharge (MSD) evolving in time and propagating in space as shown in Figure 25 was observed for Helium gas where the ion mass is small [79]. The formation of a MSD is attributed to the local ion movement under two opposite neighbouring electric fields, that is, an electric field pointing away from the surface due to the residual positive change from multipactor discharge and another electric field pointing towards the surface from electron ambipolar diffusion in space. It is worth noting that studies on breakdown in light mass gas can be of interest due to the important applications of

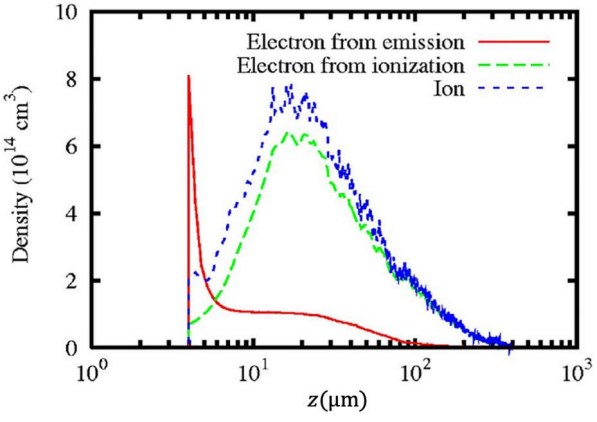

FIGURE 24 The electron and ion density profile in space for ionization breakdown at 10 Torr argon gas for transverse electric field amplitude 2.82 MV/m and frequency 2.85 GHz [88].

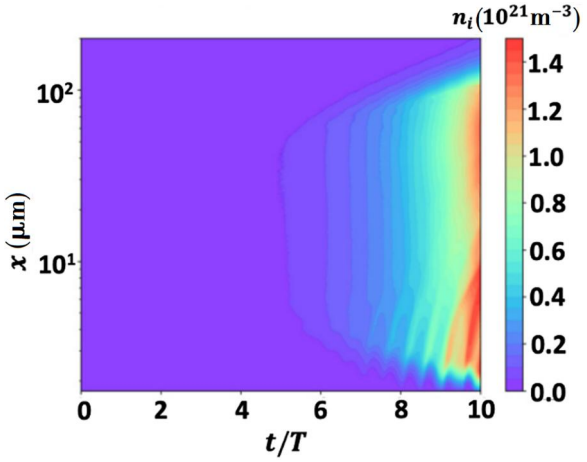

FIGURE 25 Spatiotemporal plots of the ion density in multilayer structured helium discharges [79]. T is rf period.

HPM in space-based communication satellites usually running in complicated space environments like solar wind and the proton/electron belt. It implies the light mass particles (helium and proton) can be adsorbed to the rf window initially and desorbed to a background gas due to surface heating. In the MSD, the local density near the dielectric surface can grow more rapidly than pure electron ionization breakdown, and this regime can induce a shorter breakdown time [178].

In multipactor-induced argon plasma breakdown, an enhanced higher harmonic spectrum of the normal electric field perpendicular to the tangential RF electric field was discovered [78] (see Figure 26). The higher harmonic phenomenon has a transition from presence to absence near 0.8 Torr with increasing pressure, and weakly depends on the tangential electric field in the range of 2–5 MV/m [187]. A theoretical model indicates the secondary electron streamer injecting into the bulk plasma and its interaction with bulk electrons induced instability is the underlying mechanism. It shows potential to develop a field frequency spectrum-based diagnostic of the fine transient plasma dynamics within one rf period.

6 | CONCLUSION AND OUTLOOK

For its many adverse effects, multipactor is generally undesirable in most rf applications. Concerted efforts are being made to enhance our abilities in predicting, characterising, and mitigating multipactor. In this article, the research efforts on multipactor discharge are reviewed for both single- and two-surface geometries, highlighting recent advances. An overview of basic concepts such as secondary electron emission, electron kinetics under the force law, multipactor susceptibility, and saturation mechanism is provided. Multipactor mitigation strategies with device engineering, including modern surface coating technologies, surface conditioning/scrubbing, and geometric modification by introducing artificial surface roughness and surface porosities are discussed. Device engineering is a promising approach for mitigating multipactor in future applications. Significant attention and resources are also being rendered towards mitigating multipactor in existing rf systems where massive structural overhaul might be impractical. In addition to applying external electric and magnetic fields, using engineered waveforms of the rf fields can be a viable mitigation approach in such applications. Specific configurations of two-frequency sinusoidal rf fields can mitigate multipactor strength in single surface geometry and reduce multipactor susceptibility in two-surface geometry. Non-sinusoidal Gaussian type rf operation can mitigate single surface multipactor by orders of magnitude.

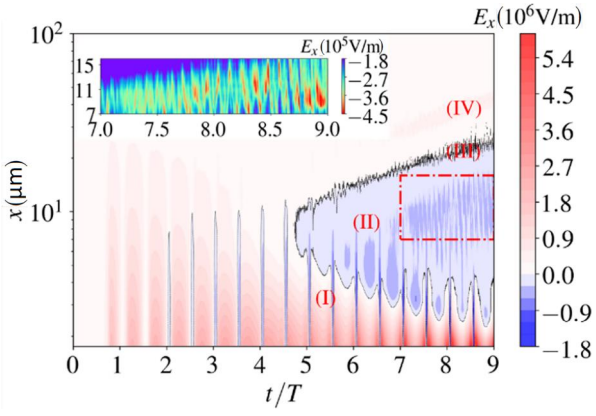

FIGURE 26 Spatiotemporal plots of the normal electric field transverse to the externally applied tangential electric field for argon plasma breakdown [78]. Horizontal and vertical axes are the time normalised to the rf period T and the distance away from the surface. The subplot on the left top corner is the zoomed plot of the region within the red box.

The past decade has been marked by several important new discoveries in the multipactor physics and engineering front. The European Cooperation for Space Standardisation (ECSS) has recently updated its multicarrier multipaction prediction methods after almost 2 decades. The new methods, while empirical in nature, are simple, accurate enough, and suitable for industry standards. The effects of space charge has been understood with the help of increased computational capabilities. Space charge introduces effects such as the virtual cathode formation, disruption of resonant electron motion, and reduction of the primary electron's impact energy onto the surface which can result in a shrinkage of multipactor susceptibility bands. Frequency domain analyses have revealed that harmonics and subharmonics of the single– and multi-frequency driving rf voltage may be generated in multipactor discharge. Therefore, higher harmonic generation can be considered as a potential application of multipactor. Schemes to control the migration of multipacting electron trajectories have been proposed for both single- and two-surface geometries. Many of these recent discoveries are yet to be validated.

In terms of volume breakdown, we reviewed the earlier findings and recent progresses that provide deeper understanding into the physics from multipactor to rf plasma formation. We revisited the early findings in current, illumination properties, X-ray emission, the gas desorption from the surface, the microwave breakdown threshold on the upstream and down stream side, as well as the discharge properties in microsecond/nanosecond pulse high power microwave systems. We also discussed the ionization breakdown time in a wide range of pressure, and the plasma filamentation phenomenon in air breakdown. In addition, the recent findings of the multilayer-structured discharge and enhanced higher harmonic frequency spectrum of the normal electric field transverse to the applied tangential rf electric field are summarised. Even though much more understanding about the plasma breakdown has been accumulated in the past decade, a fully kinetic particle-based simulation for the whole rf window in 2D is still desirable with the progress in computational capability. Diagnostics from experiments into the transient plasma process near a rf window are still challenging due to the small scale in space (micrometre to millimetre) and high resolution in time (sub-nanosecond), and modelling is often the only available method for investigation at that scale.

Although multipactor is generally considered problematic in most applications, potential beneficial applications include high power microwave switches [188, 189], surface cleaning

[60, 132, 190], and harmonic generation [150, 151]. Further studies in this regard might be of great interest to the rf community.

ACKNOWLEDGEMENTS

This work was supported by the Air Force of Scientific Research (AFOSR) MURI under Grant Nos. FA9550-18-1-0062 and FA9550-21-1-0367.

CONFLICT OF INTEREST STATEMENT

The authors declare that they have no known competing financial interests or personal relationships that could have appeared to influence the work reported in this paper.

DATA AVAILABILITY STATEMENT

The data that support the findings of this study are available from the corresponding author upon reasonable request.

ORCID

Asif Iqbal https://orcid.org/0000-0001-7460-3339
De-Qi Wen https://orcid.org/0000-0002-2662-9777
John Verboncoeur https://orcid.org/0000-0002-7078-3544
Peng Zhang https://orcid.org/0000-0003-0606-6855

REFERENCES

1. Farnsworth, P.T.: Television by electron image scanning. J. Frankl. Inst. 218(4), 411–444 (1934)
2. Vaughan, J.R.M.: Multipactor. IEEE Trans. Electron. Devices 35(7), 1172–1180 (1988)
3. Kishek, R.A., et al.: Multipactor discharge on metals and dielectrics: historical review and recent theories. Phys. Plasmas 5, 2120–2126 (1998)
4. Kishek, R.A.: Interaction of Multipactor Discharge and rf Structures. Dissertation, University of Michigan (1997)
5. Valfells, A.: Multipactor Discharge: Frequency Response, Suppression, and Relation to Window Breakdown. Dissertation, University of Michigan (2000)
6. Kishek, R.A., Lau, Y.Y.: Multipactor discharge on a dielectric. Phys. Rev. Lett. 80(1), 193–196 (1998)
7. Schaub, S.C., Shapiro, M.A., Temkin, R.J.: Measurement of dielectric multipactor thresholds at 110 GHz. Phys. Rev. Lett. 123(17), 175001 (2019)
8. Bruining, H., De Boer, J.H., Burgers, W.G.: Secondary electron emission of soot in valves with oxidecathode. Physica 4, 267–275 (1937)
9. Dekker, A.J.: Secondary electron emission. In: Seitz, F., Turnbull, D. (eds.) Solid State Physics, vol. 6, pp. 251–311. Academic Press (1958)
10. Vaughan, J.R.M.: A new formula for secondary emission yield. IEEE Trans. Electron. Devices 36(9), 1963–1967 (1989)
11. Furman, M., Pivi, M.: Probabilistic model for the simulation of secondary electron emission. Phys. Rev. Spec. Top. Accel. Beams 5(12), 124404 (2002)
12. Gonzalez-Iglesias, D., et al.: Novel multipactor studies in RF satellite payloads: single-carrier digital modulated signals and ferrite materials. In: 2017 IEEE MTT-S International Conference on Numerical Electromagnetic and Multiphysics Modeling and Optimization for RF, Microwave, and Terahertz Applications (NEMO), pp. 248–250. IEEE, Seville (2017)
13. Nagesh, S.K., Revannasiddiah, D., Shastry, S.V.K.: Investigation of multipactor breakdown in communication satellite microwave Co-axial systems. Pramana 64(1), 95–110 (2005)
14. Graves, T.P., Hubble, A.A., Partridge, P.T.: Physics-based standard for RF breakdown prevention in spacecraft components. In: 2016 IEEE International Conference on Plasma Science (ICOPS) (2016).1
15. Wong, P., Zhang, P., Luginsland, J.: Recent theory of traveling-wave tubes: a tutorial-review. Plasma Res. Express 2, 023001 (2020)
16. Benford, J., Swegle, J.A., Schamiloglu, E.: High Power Microwaves, 3rd ed. CRC Press (2015)
17. Rice, S.A.: Multipactor in the Presence of Higher-order Modes: A Numerical Study. Dissertation, Michigan State University (2017)
18. Bruning, O., et al.: Electron cloud and beam scrubbing in the LHC. In: Proceedings of the 1999 Particle Accelerator Conference (Cat. No.99CH36366), vol. 4, pp. 2629–2631. IEEE, New York (1999)
19. Zhang, S.Y., et al.: Beam scrubbing strategy for electron-cloud suppression in the spallation neutron source ring. In: Proceedings of the 2003 Bipolar/BiCMOS Circuits and Technology Meeting (IEEE Cat. No.03CH37440), vol. 5, pp. 3419–3421. IEEE, Portland (2003)
20. Preist, D.H., Talcott, R.C.: On the heating of output windows of microwave tubes by electron bombardment. IRE Trans. Electron. Devices 8(4), 243–251 (1961)
21. Vaughan, J.R.M.: Some high-power window failures. IRE Trans. Electron. Devices 8(4), 302–308 (1961)
22. Yamaguchi, S., et al.: Trajectory simulation of multipactoring electrons in an S-band pillbox RF window. IEEE Trans. Nucl. Sci. 39(2), 278–282 (1992)
23. Neuber, A., et al.: Window breakdown caused by high-power microwaves. IEEE Trans. Plasma Sci. 26(3), 296–303 (1998)
24. Wong, P.Y., et al.: The effects of multipactor on the quality of a complex signal propagating in a transmission line. Phys. Plasmas 26(11), 112114 (2019)
25. Graves, T.P.: Experimental Investigation of Electron Multipactor Discharges at Very High Frequency. Dissertation, Massachusetts Institute of Technology (2006)
26. Bellunato, A.: Experimental Study on the Electron Multipacting and Surface Conditioning. CERN (VSC_SCC), Geneva (2014). https://indico.cern.ch/event/304586/contributions/699805/attachments/577466/795281/Amedeo_Bellunato-_Multipacting_Seminar.pdf
27. Aldan, M.T.P.: Modeling and Simulation of Electrical Breakdown in DC for Dielectric-Loaded Systems with Non-Orthogonal Boundaries Including the Effects of Space-Charge and Gaseous Collisions. Dissertation, University of California (2015)
28. Gutton, C., Gutton, H.: Sur la décharge électrique en haute fréquence. Compt. Rend. 186(303) (1928)
29. Farnsworth, P.T.: Multipactor (1938). Technical Report 2135615
30. Farnsworth, P.T.: Multipactor Oscillator (1938). Technical Report 2137528
31. Farnsworth, P.T.: Multipactor Oscillator and Amplifier (1937). Technical Report 2091439
32. Farnsworth, P.T.: Multipactor Phase Control (1938). Technical Report 2071517
33. Gill, E.W.B., von Engel, A.: Starting potentials of high-frequency gas discharges at low pressure. Proc. R. Soc. Lond. Ser. Math. Phys. Sci. 192, 446 (1948)
34. Hatch, A.J., Williams, H.B.: The secondary electron resonance mechanism of low-pressure high-frequency gas breakdown. J. Appl. Phys. 25(4), 417–423 (1954)
35. Hatch, A.J., Williams, H.B.: Multipacting modes of high-frequency gaseous breakdown. Phys. Rev. 112(3), 681–685 (1958)
36. Henneburg, W., Orthuber, R., Steudel, E.: Zur wirkungsweise des elektronenvervielfachers. Z. Tech. Phys. 17, 115 (1936)
37. Riyopoulos, S.: Multipactor saturation due to space-charge-induced debunching. Phys. Plasmas 4(5), 1448–1462 (1997)
38. Riyopoulos, S., Chernin, D., Dialetis, D.: Theory of electron multipactor in crossed fields. Phys. Plasmas 2(8), 21–3213 (1995)
39. Riyopoulos, S., Chernin, D., Dialetis, D.: Effect of random secondary delay times and emission velocities in electron multipactors. IEEE Trans. Electron. Devices 44(3), 489–497 (1997)
40. Kishek, R., Lau, Y.Y.: Interaction of multipactor discharge and rf circuit. Phys. Rev. Lett. 75(6), 1218–1221 (1995)
41. Kishek, R.A., Lau, Y.Y.: A novel phase focusing mechanism in multipactor discharge. Phys. Plasmas 3(5), 1481–1483 (1996)
42. Kishek, R.A., Lau, Y.Y., Chernin, D.: Steady state multipactor and dependence on material properties. Phys. Plasmas 4(3), 863–872 (1997)

43. Ang, L.-K., et al.: Power deposited on a dielectric by multipactor. IEEE Trans. Plasma Sci. 26(3), 290–295 (1998)
44. Valfells, A., Verboncoeur, J.P., Lau, Y.Y.: Space-charge effects on multipactor on a dielectric. IEEE Trans. Plasma Sci. 28(3), 529–536 (2000)
45. Valfells, A., et al.: Effects of an external magnetic field, and of oblique radio-frequency electric fields on multipactor discharge on a dielectric. Phys. Plasmas 7(2), 750–757 (2000)
46. Anza, S., et al.: Nonstationary statistical theory for multipactor. Phys. Plasmas 17(6), 062110 (2010)
47. Anza, S., et al.: Prediction of multipactor breakdown for multicarrier applications: the quasi-stationary method. IEEE Trans. Microw. Theor. Tech. 60(7), 2093–2105 (2012)
48. Anza, S., et al.: Multipactor theory for multicarrier signals. Phys. Plasmas 18(3), 032105 (2011)
49. Anza, S., et al.: Long-term multipactor discharge in multicarrier systems. Phys. Plasmas 14(8), 082112 (2007)
50. Anza, S., et al.: Multipactor prediction with multi-carrier signals: experimental results and discussions on the 20-gap-crossing rule. In: 8th European Conference on Antennas and Propagation (EuCAP), pp. 1638–1642. IEEE, The Hague (2014)
51. Anza, S., et al.: Experimental verification of multipactor prediction methods in multicarrier systems. In: 46th European Microwave Conference (EuMC), pp. 226–229. IEEE, London (2016)
52. Vdovicheva, N.K., Sazontov, A.G., Semenov, V.E.: Statistical theory of two-sided multipactor. Radiophys. Quantum Electron. 47(8), 580–596 (2004)
53. Sazontov, A., et al.: Multipactor discharge on a dielectric surface: statistical theory and simulation results. Phys. Plasmas 12(9), 093501 (2005)
54. Lin, S., et al.: Multipactor threshold calculation of coaxial transmission lines in microwave applications with nonstationary statistical theory. Phys. Plasmas 22(8), 082114 (2015)
55. Siddiqi, M., Kishek, R.: Map-based multipactor theory for cross-field devices. IEEE Trans. Electron. Devices 66(7), 3162–3167 (2019)
56. Siddiqi, M., Kishek, R.: Construction of multipactor susceptibility diagrams from map-based theory. IEEE Trans. Electron. Devices 66(8), 3587–3591 (2019)
57. European Corporation for Space Standardization (ECSS): Space Engineering: Multipacting Design and Test. ESA Publication Division (2013)
58. Zhang, P., et al.: Multipactor susceptibility on a dielectric with a bias dc electric field and a background gas. Phys. Plasmas 18(5), 053508 (2011)
59. Iqbal, A., Verboncoeur, J., Zhang, P.: Multipactor susceptibility on a dielectric with two carrier frequencies. Phys. Plasmas 25(4), 043501 (2018)
60. Iqbal, A., et al.: Time-dependent physics of single-surface multipactor discharge with two carrier frequencies. Phys. Rev. E 102(4), 043201 (2020)
61. Kim, H.C., Verboncoeur, J.P.: Time-dependent physics of a single-surface multipactor discharge. Phys. Plasmas 12, 123504 (2005)
62. Iqbal, A., et al.: A review of recent studies on two-frequency RF field-induced single-surface multipactor discharge. IEEE Trans. Plasma Sci. 49(11), 3284–3292 (2021)
63. Li, Y., et al.: MSAT: a novel multipactor simulation and analysis tool. In: 2018 International Conference on Microwave and Millimeter Wave Technology (ICMMT), pp. 1–3 (2018)
64. Li, Y., et al.: Three-dimensional simulation method of multipactor in microwave components for high-power space application. Chin. Phys. B 23(4), 048402 (2014)
65. de Lara, J., et al.: Multipactor prediction for on-board spacecraft RF equipment with the MEST software tool. IEEE Trans. Plasma Sci. 34(2), 476–484 (2006)
66. Pérez, F., et al.: Simulation of multipactor effect through the individual simulation of electrons. In: 5th International Workshop on Multipactor, Corona and Passive Intermodulation in Space RF Hardware (MULCOPIM 2005), pp. 267–273. Noordwijk, The Netherlands (2005)
67. Vicente, C.C., et al.: FEST3D - a simulation tool for multipactor prediction. In: Proc. 5th Int. Workshop MULCOPIM (2005)
68. Anza, S., et al.: Enhanced prediction of multipaction breakdown in passive waveguide components including space charge effects. In: 2008 IEEE MTT-S International Microwave Symposium Digest, pp. 1095–1098 (2008)
69. Al Hajj Sleiman, E., et al.: Evaluation of multipactor thresholds for coaxial lines subject to surface conditioning for the WEST ion cyclotron antenna. Fusion Eng. Des. 185, 113325 (2022)
70. Burt, G., et al.: Benchmarking simulations of multipactor in rectangular waveguides using CST-particle studio. In: Proceedings of 14th International Conference on RF Superconductivity (SRF2009), pp. 321–325. Berlin (2009)
71. Romanov, G.: Update on multipactor in coaxial waveguides using CST particle studio. In: Proceedings of 2011 Particle Accelerator Conference, pp. 820–822. New York (2011)
72. Langellotti, S.V., et al.: CST particle studio simulations of coaxial multipactor and comparison with experiments. IEEE Trans. Plasma Sci. 48(6), 1942–1949 (2020)
73. Langellotti, S.V., et al.: Multipactor experiments on an S-band coaxial test cell. Rev. Sci. Instrum. 92(12), 124706 (2021)
74. Neuber, A., et al.: Initiation of high power microwave dielectric interface breakdown. J. Appl. Phys. 86(3), 1724–1728 (1999)
75. Chang, C., et al.: Ultrafast high-power microwave window breakdown: nonlinear and postpulse effects. Phys. Rev. E 90(6), 063107 (2014)
76. Nam, S.K., Verboncoeur, J.P.: Theory of filamentary plasma array formation in microwave breakdown at near-atmospheric pressure. Phys. Rev. Lett. 103(5), 055004 (2009)
77. Boeuf, J.-P., Chaudhury, B., Zhu, G.Q.: Theory and modeling of self-organization and propagation of filamentary plasma arrays in microwave breakdown at atmospheric pressure. Phys. Rev. Lett. 104(1), 015002 (2010)
78. Wen, D.-Q., et al.: Higher harmonics in multipactor induced plasma ionization breakdown near a dielectric surface. Phys. Rev. Lett. 129(4), 045001 (2022)
79. Wen, D.-Q., et al.: Observation of multilayer-structured discharge in plasma ionization breakdown. Appl. Phys. Lett. 119(26), 264102 (2021)
80. Vaughan, R.M.: Secondary emission formulas. IEEE Trans. Electron. Devices 40(4), 830 (1993)
81. Shih, A., et al.: Secondary electron emission studies. Appl. Surf. Sci. 111, 251–258 (1997)
82. Rice, S.A., VerboncoeurIEEE, J.P.: A comparison of multipactor predictions using two popular secondary electron models. IEEE Trans. Plasma Sci. 42(6), 1484–1487 (2014)
83. Gutierrez, R.E., et al.: First principles inelastic mean free paths coupled with Monte Carlo simulation of secondary electron yield of Cu-Ni, Cu-Zn, and Mo-Li. J. Appl. Phys. 129(17), 175105 (2021)
84. Iqbal, A.: Multipactor Discharge with Two-Frequency RF Fields. Dissertation, Michigan State University (2021)
85. Sorolla Rosario, F.E.: Contribution to Modeling Multipactor and Corona Discharges in High Power Electromagnetic Fields. Swiss Federal Institute of Technology (EPFL) (2012)
86. Gopinath, V.P., Verboncoeur, J.P., Birdsall, C.K.: Multipactor electron discharge physics using an improved secondary emission model. Phys. Plasmas 5, 1535–1540 (1998)
87. Iqbal, A., Verboncoeur, J., Zhang, P.: Temporal multiparticle Monte Carlo simulation of dual frequency single surface multipactor. Phys. Plasmas 26(2), 024503 (2019)
88. Kim, H.C., Verboncoeur, J.P.: Transition of window breakdown from vacuum multipactor discharge to Rf plasma. Phys. Plasmas 13(12), 123506 (2006)
89. Woo, R.: Multipacting discharges between coaxial electrodes. J. Appl. Phys. 39(3), 1528–1533 (1968)
90. Woo, R.: Multipacting breakdown in coaxial transmission lines. Proc. IEEE 56(4), 776–777 (1968)
91. Woo, R., Ishimaru, A.: A similarity principle for multipacting discharges. J. Appl. Phys. 38(13), 5240–5244 (1967)
92. Udiljak, R., et al.: Multipactor in a coaxial transmission line. I. Analytical study. Phys. Plasmas 14(3), 033508 (2007)
93. Semenov, V.E., et al.: Multipactor in a coaxial transmission line. II. Particle-in-Cell simulations. Phys. Plasmas 14(3), 033509 (2007)
94. Siddiqi, M., Kishek, R.: A predictive model for multipactor discharge in coaxial systems based on chaos theory. IEEE Trans. Electron. Devices 66(10), 4403–4407 (2019)

95. Sorolla, E., Sounas, A., Mattes, M.: Space charge effects for multipactor in coaxial lines. Phys. Plasmas 22(3), 033512 (2015)
96. Romanov, G.: Simulation of multipacting with space charge effect. Am. J. Phys. Appl. 5(6), 99 (2017)
97. Tang, Y., et al.: Multipacting study for fundamental power coupler of a superconducting cavity. J. Instrum. 18(1), P01026 (2023)
98. Hayes, R.: Research on Microwave Window Multipactor and its Inhibition, No. Defense Technical Information Center, AD0456965. EITEL-MCCULLOUGH INC (1964)
99. Joy, D.C.: A database on electron-solid interactions. Scanning 17(5), 270–275 (1995)
100. Bruining, H.: Secondary electron emission. Philips Tech. Rev. 3, 80 (1938)
101. Jonker, J.L.H.: Phenomena in amplifier valves caused by secondary emission. Philips Tech. Rev. 3, 211 (1938)
102. Rimmer, R.A.: High Power Microwave Window Failures. Dissertation, Lancaster University (1988)
103. Lyneis, C.M., Schwettman, H.A., Turneaure, J.P.: Elimination on electron multipacting in superconducting structures for electron accelerators. Appl. Phys. Lett. 31(8), 541–543 (1977)
104. Chang, C., et al.: Suppression of high-power microwave dielectric multipactor by resonant magnetic field. Appl. Phys. Lett. 96(11), 111502 (2010)
105. Chang, C., et al.: Experimental verification of improving high-power microwave window breakdown thresholds by resonant magnetic field. Appl. Phys. Lett. 97(14), 141501 (2010)
106. Ivanov, O.A., et al.: Suppressing and initiation of multipactor discharge on a dielectric by an external dc bias. Phys. Rev. Spec. Top. Accel. Beams 13(2), 022004 (2010)
107. Chang, C., et al.: Review of recent theories and experiments for improving high-power microwave window breakdown thresholds. Phys. Plasmas 18(5), 055702 (2011)
108. Wen, D.-Q., et al.: Susceptibility of multipactor discharges near a dielectric driven by a Gaussian-type transverse rf electric field. Appl. Phys. Lett. 121(16), 164103 (2022)
109. Chang, C., et al.: Field distribution, HPM multipactor, and plasma discharge on the periodic triangular surface. Laser Part. Beams 28(1), 185–193 (2010)
110. Nistor, V., et al.: Multipactor suppression by micro-structured gold/silver coatings for space applications. Appl. Surf. Sci. 315, 445–453 (2014)
111. Watts, C., Gilmore, M., Schamiloglu, E.: Effects of laser surface modification on secondary electron emission of copper. IEEE Trans. Plasma Sci. 39(3), 836–841 (2011)
112. Zhang, S., et al.: Modelling vacuum flashover mitigation with complex surface microstructure: mechanism and application. High Volt. 5(2), 110–121 (2020)
113. Li, S.: Improvement of surface flashover in vacuum. High Volt. 5(2), 122–133 (2020)
114. Pivi, M., et al.: Sharp reduction of the secondary electron emission yield from grooved surfaces. J. Appl. Phys. 104(10), 104904 (2008)
115. Ye, M., et al.: Suppression of secondary electron yield by micro-porous array structure. J. Appl. Phys. 113, 074904 (2013)
116. Sattler, J.M., et al.: Modeling micro-porous surfaces for secondary electron emission control to suppress multipactor. J. Appl. Phys. 122(5), 055304 (2017)
117. Iqbal, A., et al.: Empirical modeling and Monte Carlo simulation of secondary electron yield reduction of laser drilled microporous gold surfaces. J. Vac. Sci. Technol. B 38(1), 013801 (2020)
118. Ludwick, J., et al.: Angular dependence of secondary electron yield from microporous gold surfaces. J. Vac. Sci. Technol. B 38(5), 054001 (2020)
119. Mirmozafari, M., et al.: Secondary electron yield characterization of high porosity surfaces for multipactor-free microwave components. Phys. Plasmas 29(8), 082109 (2022)
120. Mirmozafari, M., Behdad, N., Booske, J.H.: Calculating multipactor susceptibility chart using a semi-analytic approach with improved accuracy. Phys. Plasmas 27(11), 113510 (2020)
121. Zhai, Y., et al.: Effect of secondary emission yield and initial charge of dielectric material on multipactor in parallel-plate dielectric-loaded waveguide. IEEE Trans. Electron. Devices 66(12), 5333–5338 (2019)
122. Zhang, X., Yu, Q., Ni, X.: Saturation mechanism of multipactor effect in a one-sided dielectric-loaded waveguide. IEEE Trans. Electron. Devices 69(2), 748–753 (2022)
123. Yin Vallgren, C., et al.: Amorphous carbon coatings for the mitigation of electron cloud in the CERN super proton Synchrotron. Phys. Rev. Spec. Top. Accel. Beams 14(7), 071001 (2011)
124. Eldred, J., et al.: Beam Tests of Diamond-Like Carbon Coating for Mitigation of Electron Cloud, pp. 4497–4500. JACoW, Copenhagen (2017)
125. Nguyen, H.K.A., et al.: Calculations of secondary electron yield of graphene coated copper for vacuum electronic applications. AIP Adv. 8(1), 015325 (2018)
126. Yang, J., et al.: Nanofabrication techniques used for suppressing multipactor in space applications. In: 2018 IEEE International Conference on Manipulation, Manufacturing and Measurement on the Nanoscale (3M-NANO), pp. 241–244. Hangzhou, China (2018)
127. Wang, J., et al.: Secondary electron emission characteristics of graphene films with copper substrate. Chin. Phys. C 40(11), 117003 (2016)
128. Feng, G., et al.: Gas desorption and secondary electron emission from graphene coated copper due to E-beam stimulation. Coatings 13(2), 370 (2023)
129. Wu, D., et al.: Fabrication of porous Ag/TiO_2/Au coatings with excellent multipactor suppression. Sci. Rep. 7, 43749 (2017)
130. Martínez, B.G.: Recent advances on multipactor effect in satellites communications RF. In: Joint INFN-CERN-ARIES Workshop on Electron-Cloud Effects (ECLOUD'18), La Biodola, Isola d'Elba, Italy (2018). https://agenda.infn.it/event/13351/contributions/18975/attachments/13638/15344/ecloud2018_BGM_Valencia.pdf
131. Iqbal, A., Verboncoeur, J., Zhang, P.: Two surface multipactor discharge with two-frequency rf fields and space-charge effects. Phys. Plasmas 29(1), 012102 (2022)
132. Rice, S.A., Verboncoeur, J.P.: Migration of multipactor trajectories via higher-order mode perturbation. IEEE Trans. Plasma Sci. 45(7), 1739–1745 (2017)
133. Wen, D.-Q., et al.: Suppression of single-surface multipactor discharges due to non-sinusoidal transverse electric field. Phys. Plasmas 26(9), 093503 (2019)
134. European Corporation for Space Standardization (ECSS): Multipaction Design and Test. ESA Publication Division (2003). https://ecss.nl/standard/ecss-e-20-01a-multipaction-design-and-test-5-may-2003/
135. European Corporation for Space Standardization (ECSS): Multipaction Design and Test. ESA Publication Division (2020). https://ecss.nl/standard/ecss-e-st-20-01c-multipactor-design-and-test-15-june-2020/
136. Anza, S., et al.: Novel prediction methods of multicarrier multipactor for space industry standards. IEEE Trans. Microw. Theor. Tech. 70(1), 670–684 (2022)
137. Chang, C., et al.: The influence of space charge shielding on dielectric multipactor. Phys. Plasmas 16(5), 053506 (2009)
138. Lingwood, C.J., et al.: Phase space analysis of multipactor saturation in rectangular waveguide. Phys. Plasmas 19(3), 032106 (2012)
139. Coves, Á., et al.: Multipactor discharges in parallel-plate dielectric-loaded waveguides including space-charge effects. IEEE Trans. Electron. Devices 55(9), 2505–2511 (2008)
140. Fowler, R.H., Nordheim, L.: Electron emission in intense electric fields. Proc. R. Soc. Lond. - Ser. A Contain. Pap. a Math. Phys. Character 119, 173 (1928)
141. Zhang, P., et al.: Field emission from carbon nanotube fibers in varying anode-cathode gap with the consideration of contact resistance. AIP Adv. 7(12), 125203 (2017)
142. Lin, J., et al.: Electric field distribution and current emission in a miniaturized geometrical diode. J. Appl. Phys. 121(24), 244301 (2017)
143. Zhang, P., Lau, Y.Y.: Ultrafast strong-field photoelectron emission from biased metal surfaces: exact solution to time-dependent schrödinger equation. Sci. Rep. 6(1), 19894 (2016)

144. Zhou, Y., Zhang, P.: A quantum model for photoemission from metal surfaces and its comparison with the three-step model and Fowler–DuBridge model. J. Appl. Phys. 127(16), 164903 (2020)
145. Zhou, Y., Zhang, P.: Quantum efficiency of photoemission from biased metal surfaces with laser wavelengths from UV to NIR. J. Appl. Phys. 130(6), 064902 (2021)
146. Wen, D.-Q., et al.: Temporal single-surface multipactor dynamics under obliquely incident linearly polarized electric field. Phys. Plasmas 26(12), 123509 (2019)
147. Zhang, Z., et al.: An analytical model of one-sided multipactor on a dielectric of a metal surface for spacecraft application. IEEE Trans. Electron. Devices 66(11), 4921–4927 (2019)
148. Zhang, L., et al.: Numerical simulation and analysis of passive intermodulation caused by multipaction. Phys. Plasmas 25(8), 082301 (2018)
149. Yang, H., et al.: An analytical method to evaluate the spectrum of multicarrier multipactor discharge. IEEE Trans. Electron. Devices 68(4), 1918–1923 (2021)
150. Wong, P.Y., Zhang, P., Verboncoeur, J.P.: Harmonic generation in multipactor discharges. IEEE Trans. Plasma Sci. 48(6), 1959–1966 (2020)
151. Iqbal, A., et al.: Frequency-domain analysis of single-surface multipactor discharge with single- and dual-tone RF electric fields. IEEE Trans. Plasma Sci. 48(6), 1950–1958 (2020)
152. Mirmozafari, M., Behdad, N., Booske, J.H.: Ultrawideband, high-power, microstripline test setup for experimental study and characterization of multipactor. Rev. Sci. Instrum. 92(8), 084706 (2021)
153. Shaw, Z.C., et al.: On the limits of multipactor in rectangular waveguides. Phys. Plasmas 27(8), 083512 (2020)
154. Vague, J., et al.: Multipactor effect characterization of dielectric materials for space applications. IEEE Trans. Microw. Theor. Tech. 66(8), 3644–3655 (2018)
155. Lee, Y.-S.: Principles of Terahertz Science and Technology. Springer Science & Business Media, New York (2009)
156. Fokin, A., et al.: High-power sub-terahertz source with a record frequency stability at up to 1 Hz. Sci. Rep. 8, 4317 (2018)
157. Booske, J.H.: Plasma physics and related challenges of millimeter-wave-to-terahertz and high power microwave generation. Phys. Plasmas 15(5), 055502 (2008)
158. Federici, J., Moeller, L.: Review of terahertz and subterahertz wireless communications. J. Appl. Phys. 107(11), 111101 (2010)
159. Sengupta, K., Nagatsuma, T., Mittleman, D.M.: Terahertz integrated electronic and hybrid electronic–photonic systems. Nat. Electron. 1, 622–635 (2018)
160. Xie, J., et al.: A review on terahertz technologies accelerated by silicon photonics. Nanomaterials 11(7), 1646 (2021)
161. Tonouchi, M.: Cutting-edge terahertz technology. Nat. Photonics 1, 97–105 (2007)
162. Power, J.G., et al.: Observation of multipactor in an alumina-based dielectric-loaded accelerating structure. Phys. Rev. Lett. 92(16), 164801 (2004)
163. Sakharov, A.S., et al.: Theoretical and experimental study of microwave power absorption by a single-sided multipactor discharge on a dielectric. Plasma Phys. Rep. 38(13), 1090–1098 (2012)
164. Anderson, R.B., et al.: Multipactor experiment on a dielectric surface. Rev. Sci. Instrum. 72(7), 3095–3099 (2001)
165. Sorolla, E., et al.: An analytical model to evaluate the radiated power spectrum of a multipactor discharge in a parallel-plate region. IEEE Trans. Electron. Devices 55(8), 2252–2258 (2008)
166. Jiménez, M., et al.: Analysis of the electromagnetic radiation generated by a multipactor discharge occurring within a microwave passive component. J. Phys. Appl. Phys. 43(39), 395501 (2010)
167. Semenov, V.E., et al.: Simple model of the Rf noise generated by multipacting electrons. J. Phys. Appl. Phys. 47(5), 055206 (2014)
168. Wang, X., et al.: Monte Carlo analysis of occurrence thresholds of multicarrier multipactors. IEEE Trans. Microw. Theor. Tech. 65(8), 2734–2748 (2017)
169. Anderson, R.A., Brainard, J.P.: Mechanism of pulsed surface flashover involving electron-stimulated desorption. J. Appl. Phys. 51(3), 1414–1421 (1980)
170. Miller, H.C.: Surface flashover of insulators. IEEE Trans. Electr. Insul. 24(5), 765–786 (1989)
171. Hegeler, F., et al.: Current, luminosity, and X-ray emission in the early phase of dielectric surface flashover in vacuum. IEEE Trans. Plasma Sci. 21(2), 223–227 (1993)
172. Lehr, M., et al.: Magnetic-field effects on vacuum insulator flashover. J. Appl. Phys. 71(1), 389–394 (1992)
173. Neuber, A.A., et al.: The role of outgassing in surface flashover under vacuum. IEEE Trans. Plasma Sci. 28(5), 1593–1598 (2000)
174. Hemmert, D., et al.: Microwave magnetic field effects on high-power microwave window breakdown. IEEE Trans. Plasma Sci. 28(3), 472–477 (2000)
175. Hidaka, Y., et al.: Observation of large arrays of plasma filaments in air breakdown by 1.5-MW 110-GHz gyrotron pulses. Phys. Rev. Lett. 100(3), 035003 (2008)
176. Zhou, Q., Dong, Z.: Modeling study on pressure dependence of plasma structure and formation in 110 GHz microwave air breakdown. Appl. Phys. Lett. 98(16), 161504 (2011)
177. Krile, J.T., et al.: Monte Carlo simulation of high power microwave window breakdown at atmospheric conditions. Appl. Phys. Lett. 89(20), 201501 (2006)
178. Lau, Y.Y., Verboncoeur, J.P., Kim, H.C.: Scaling laws for dielectric window breakdown in vacuum and collisional regimes. Appl. Phys. Lett. 89(26), 261501 (2006)
179. Nam, S.K., Verboncoeur, J.P.: Effect of electron energy distribution function on the global model for high power microwave breakdown at high pressures. Appl. Phys. Lett. 92(23), 231502 (2008)
180. Nam, S.K., Verboncoeur, J.P.: Effect of microwave frequency on breakdown and electron energy distribution function using a global model. Appl. Phys. Lett. 93(15), 151504 (2008)
181. Beeson, S., Dickens, J., Neuber, A.: Plasma relaxation mechanics of pulsed high power microwave surface flashover. Phys. Plasmas 20(9), 093509 (2013)
182. Edmiston, G.F., Krile, J.T., Neuber, A.A.: Imaging of high-power microwave-induced surface flashover on a corrugated dielectric window. IEEE Trans. Plasma Sci. 36(4), 946–947 (2008)
183. Chang, C., et al.: Diagnostic of ultrafast temporal plasma evolution in high-power microwave discharge. J. Appl. Phys. 121(21), 213301 (2017)
184. Chang, C., et al.: Enhanced window breakdown dynamics in a nanosecond microwave tail pulse. Appl. Phys. Lett. 104(25), 253504 (2014)
185. Wen, D.-Q., et al.: Benchmarked and upgraded particle-in-cell simulations of a capacitive argon discharge at intermediate pressure: the role of metastable atoms. Plasma Sources Sci. Technol. 30(10), 105009 (2021)
186. Wen, D.-Q., et al.: Particle-in-Cell simulations with fluid metastable atoms in capacitive argon discharges: electron elastic scattering and plasma density profile transition. IEEE Trans. Plasma Sci. 50(9), 2548–2557 (2022)
187. Wen, D.-Q., et al.: Parametric studies of stream instability-induced higher harmonics in plasma ionization breakdown near an emissive dielectric surface. Plasma Sources Sci. Technol. 31(9), 095004 (2022)
188. Forrer, M.P., Milazzo, C.: Duplexing and switching with multipactor discharges. Proc. IRE 50(4), 442–450 (1962)
189. Song, W., et al.: A rapid high power microwave switch based on multipactor electrons flow. Appl. Phys. Lett. 102, 013504 (2013)
190. Bourat, C., Joly, J.-M.: On multipactor effect in a 600 MHz RF cavity used in electron linear accelerator. IEEE Trans. Electr. Insul. 24(6), 1045–1048 (1989)

How to cite this article: Iqbal, A., et al.: Recent advances in multipactor physics and mitigation. High Voltage. 8(6), 1095–1114 (2023). https://doi.org/10.1049/hve2.12335